Politecnico di Torino

ScuDo
Scuola di Dottorato ~ Doctoral School
WHAT YOU ARE, TAKES YOU FAR

Doctoral Dissertation

Doctoral Program in Electrical, Electronics and Communications Engineering

(XXXV cycle)

Investigation of inductive components for power electronics applications

By

Luigi Solimene

******

Supervisors:
Prof. Carlo Stefano Ragusa
Prof. Aldo Canova

Doctoral Examination Committee:
Prof. Andrea Cristofolini, Referee, Università di Bologna
Prof. Antonino Laudani, Referee, Università degli Studi Roma Tre
Dr. Domenico Giordano, Istituto Nazionale di Ricerca Metrologica
Prof. Fabio Freschi, Politecnico di Torino
Prof. Luca Giaccone, Politecnico di Torino

Politecnico di Torino
21st December 2022

Declaration

I hereby declare that, the contents and organization of this dissertation constitute my own original work and does not compromise in any way the rights of third parties, including those relating to the security of personal data.

Luigi Solimene
21st December 2022

* This dissertation is presented in partial fulfillment of the requirements for **Ph.D. degree** in the Graduate School of Politecnico di Torino (ScuDo).

A tutte le persone importanti della mia vita:
ai miei genitori, alla mia famiglia, a Erica, ai buoni amici.

Acknowledgements

My gratitude goes to my supervisor, Prof. Carlo Stefano Ragusa, for the constant dedication and attention he always offered me. I would also like to thank my co-supervisor, Prof. Aldo Canova, for the numerous lessons I learned collaborating with him. A special mention goes to all the people of the CADEMA research group for the endless insights I received during the many and various conversations. I also thank Prof. Salvatore Musumeci for the constructive and interesting collaboration.

Abstract

The demand for high power density and highly efficient power electronics converters is increasingly pushing the optimisation of inductive components. Starting from state of the art in inductor design, this thesis proposes some newly developed considerations and concepts in the design of inductive components for power electronics applications, with a particular focus on inductors operating in DC-DC converters. The addressed challenges regard the core saturation, which is the principal limit to design optimisation, and the core loss modelling, which is extremely critical due to the biasing effect of the DC current. The problem of the optimised design of inductors for DC-DC converters also faces the high-frequency operation of the windings, which can strongly influence the total losses of the device.

The design analysis of an output inductor for a buck converter is presented. The modelling of inductors for DC-DC converters is discussed, and some considerations are proposed on the most suitable approaches depending on the specific design requirements. In addition, the critical aspects of the multi-objective design are discussed, focusing on the long computational time required. The multi-objective optimisation is approached with an artificial immune system based algorithm and enhanced with the adoption of a classifier system for the constraint evaluation. A classification system is proposed to evaluate the constraint of the configurations examined in the multi-objective optimisation process, highlighting interesting results in reducing the number of the required time-consuming computational tasks.

While some applications require a custom design of magnetic components, power electronic devices destined for mass production generally require commercially available components. In this case, the goals of high power density and high efficiency are reached by appropriately selecting the optimised part in the manufacturer catalogues. The conventional sizing approach of inductors for DC-DC converters aims to ensure the operation of the device in linear and stable conditions, overestimating

the required inductance value and thus selecting an oversized magnetic component. It is well known that the operation of inductors in partial saturation reduces the size of an inductor for a given inductance value, increasing the power density of a DC-DC converter. However, inductors operating in partial saturation require appropriate modelling that considers the non-linearity introduced by magnetic material behaviour. To this end, a method for the experimental identification of the differential inductance profile of commercial ferrite inductors is presented, also considering the effect of the overheating caused by the operative power losses. The experimental setup and the identification procedure to perform the characterisation are discussed. In addition, the modelling of the differential inductance profile is evaluated for the fast simulation of the current and voltage waveforms when the inductor operates in non-linear conditions.

The proper modelling of magnetic device properties can also be used to implement interesting control strategies for different energy conversion devices. In particular, this thesis evaluates the effectiveness of magnetic control for resonant converters, focusing on Wireless Power Transfer systems. The proposed magnetic control strategy is implemented through a controlled variable inductor. The design and modelling of a controlled variable inductor are described, and a prototype is realised and tested in an experimental Inductive Wireless Power Transfer system to verify the effectiveness of the magnetic control strategy. The regulation and supply system of the inductance value is also analysed. In conclusion, a controlled variable inductor is proposed for the regulation of a Capacitive Wireless Power Transfer system.

Contents

List of Figures

List of Tables

Chapter 1

Introduction

Electrification is a central topic of the present time. The massive amount of electrical and electronic devices influence each moment of our everyday lives. The impact of electricity will become even stronger considering the ongoing transition of the transport sector (terrestrial, aerial, naval) from internal combustion engines to electrified propulsion systems. Highly efficient power generation systems play an essential role in reducing pollutant emissions and reducing the amount of energy produced from fossil fuels. However, the impact of conversion systems on the overall efficiency of the electricity production-consumption cycle is not negligible. Electrical energy may be converted in different stages before it is employed for our disparate activities. As an example, for any battery-powered device (from a smartphone to an electric car), a conversion from alternating current (AC) to direct current (DC) is required to recharge it. In the framework of electric mobility, an electrochemical accumulator, a DC voltage source, provides the energy needed for a traction system that conventionally uses AC motors. Besides a conversion function from alternating current to direct current or vice versa, a regulation and control function of electrical quantities is also performed by electrical energy conversion systems.

Today, state of the art in conversion technology is represented by power electronic converters, which adopt semiconductor devices to implement highly efficient structures. There are several fields of applications of semiconductor power converters, as [1]:

- automotive: power supply for auxiliary systems (infotainment, power steering, electronic ignition). Supply and control of electric vehicles powertrains;

- computer science and consumer electronics: supply of low-voltage DC systems; battery charging;
- industrial motor control: speed and torque control systems;
- renewable energy production: energy conversion from renewable sources (wind, sunlight).

Besides high conversion efficiency, a further requirement for power converters is high power density. Reduced weight and size result in more comfortable and functional portable electronic devices. In transportation, reducing size and mass also allows for improved energy efficiency of propulsion systems. It is clear, therefore, that a power electronic converter has two essential requirements of high efficiency and high power density. These requirements can be met by improving the main components of a power converter. Semiconductor devices surely represent the core. The innovations in the field of semiconductors devices had exponential growth in the last 50 years. The development of MOSFET and IGBT has paved the way for the diffusion of efficient switch-mode power supply and variable speed drives. In the last years, wide bandgap materials, such as silicon carbon (SiC) and gallium nitride (GaN) devices, enabled the design of high switching frequency power converters, going towards the MHz range [2]. The improvements in the power semiconductor involve higher current and voltage ratings of these devices and lower conduction and switching losses, allowing highly efficient power electronics converters. However, a power electronic converter is not only made up of semiconductor devices. Every converter structure requires the use of passive components, and in particular magnetic elements.

1.1 Challenges for magnetic components in power electronics

All power converters have magnetic components in the form of inductors and transformers. Inductors are dynamic energy storage devices that allow the transition between different operating modes in a switching circuit, as in switch mode power supplies (SMPSs). Transformers are energy transfer devices that enable the conversion of the power from a high voltage and low current side to a lower voltage and higher current one, and vice versa. Other uses of transformers in power electronics

are related to the electrical isolation between two parts of a power circuit, or the sensing of current and voltage [3]. In recent years, the research in magnetic materials for power electronics did not have the same growth rate as semiconductor devices since the magnetic technology field had already reached a higher degree of maturity in the past. For this reason, the goals of maximising power density and efficiency should be addressed by better exploiting the available materials, which can be obtained through in-depth knowledge and modelling of their properties.

Magnetic components are manufactured through one or more windings (copper or aluminium) placed on a ferromagnetic core (normally iron-based). They are therefore made of materials with a high density, resulting in a very significant contribution to the weight of a power converter. In addition, they also account for a considerable share of the size of such devices. Increasing the switching frequencies of semiconductor devices reduces the required size of magnetic components but can lead to increased losses. The design of inductors and transformers for power electronic converters represents a significant challenge that involves the evaluation of the compromise between conflicting goals, defined by the high efficiency and the high power density requirements. The proper sizing of magnetics is fundamental, and the approach based on empirical rules of thumb is no more satisfactory. In addition, it is hard to find a standardisation strategy in the design of transformers and inductors for power converters, which often require a customised approach to reach the goals of power density and efficiency maximisation.

The bases of the design of magnetic components are the fundamental laws of electromagnetism. In addition, the knowledge of the ferromagnetic materials' properties is essential for their appropriate utilisation and exploitation. These materials exhibit highly non-linear behaviour, and the saturation of the cores has to be taken into account. Their properties are also dependent on the frequency. The operation at even increasing switching frequency also requires the analysis of high-frequency phenomena related to the windings. On the other hand, even thermal phenomena are involved in the design process since the operating temperature of a ferromagnetic material strongly influences its permeability and loss properties. In addition, suitable computational tools are required to deal with the circuit and electromagnetic field simulations involving magnetic components for power electronics.

1.2 The applications of magnetic components in power electronics

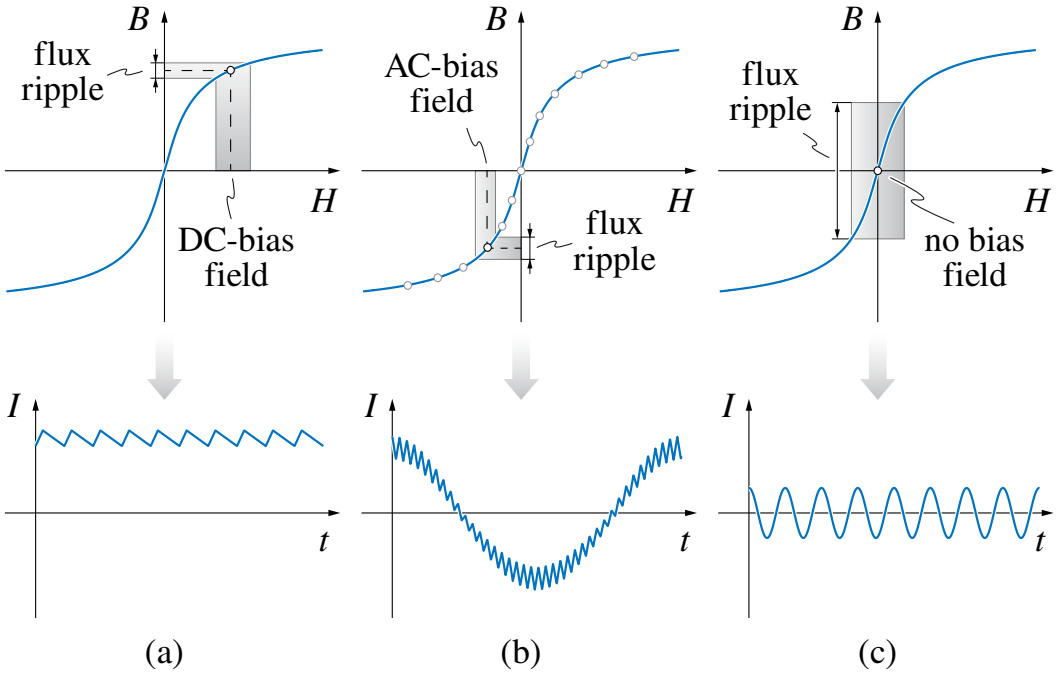

Fig. 1.1 Different operating conditions of inductor's magnetic material in power electronics applications. (a) DC bias field. (b) Low frequency AC bias field. (c) High frequency AC operation.

Different converter structures involve different operating conditions for inductive components. The applied voltage and current waveforms on inductors influence the shape of the hysteresis loop, determining the power losses and saturation behaviour of the material. Generalising, three main categories of operations can be identified, as reported in Figure 1.1:

- the high-frequency AC operation. The magnetic flux density excursion is bidirectional, and the magnetisation is reversed: This operation is not generally critical for the saturation of the core, but good specific loss properties are required to guarantee high efficiency;
- the low-frequency AC bias field operation. In this case, the magnetic flux density excursion is unidirectional, and the magnetisation is not reversed;

- the DC bias field operation. This condition involves the operation of inductors in DC-DC converters, which is the one this thesis will focus on. In this case, the saturation of the ferromagnetic material represents a criticality and should be accurately taken into account in the converter design and operation analysis.

The magnetic materials for inductor and transformer cores must be accurately selected to be suitable for the specific converter topology and operation.

1.3 The soft magnetic materials adopted for power electronics converters

Soft ferrites are the most common choice for inductors and transformers cores in power electronics applications. In particular, the Mn-Zn ferrites are employed up to the MHz range. Ferrites are ceramic materials made of iron oxide and one or more additional metallic elements, such as strontium, barium, manganese, nickel, and zinc. The non-metallic nature of this material is particularly suitable when used in a frequency range from kHz to hundreds of MHz, which includes the areas of application of power converters. These characteristics are explained by the ionic, non-metallic nature, which makes the material electrically insulating, with a resistivity of several orders of magnitude higher than other soft magnetic materials such as Fe-Si alloys and amorphous materials. This property is fundamental in using the material in high-frequency applications, for which the eddy current losses represent a significant problem. The main drawback of adopting ferrites in inductors and transformers for power electronics is the low saturation flux density (0.3 - 0.4 T) that limits their use in high current applications. In addition, ferrites have a sharp differential permeability profile. The sintering process of ferrites allows several core shapes (toroid, E, C, planar E).

Magnetic powder materials are produced from magnetic alloy grains bound together with an insulating material, resulting in the distributed air gap property. The magnetic alloys used for powder cores include combinations of iron, silicon, nickel, aluminium, borum, and molybdenum. The saturation flux density is considerably higher than ferrites (up to 1.5 T), and the differential permeability profile exhibits a gradual saturation, with a predictable behaviour even at high values of applied magnetic fields. Magnetic powder cores are typically operated in the ungapped

configuration and are available in several shapes as ferrites. Metal powder cores are particularly attractive in high current applications up to the tens of kHz range.

The amorphous alloys are obtained after rapid cooling of molten metallic alloys, including various concentrations of iron, cobalt, nickel, and silicon and boron to decrease the alloy's melting point. They are produced as a tape with a thickness of a few tens of micrometres, and then they are formed as toroids or C-cut cores. The resistivity of amorphous alloys is higher than silicon steel but considerably lower than ferrites. However, the losses are reduced through extremely thin lamination. The saturation flux density and the relative permeability are high (up to 1.6 T and 100000, respectively). Nanocrystalline materials are obtained through heat treatment applied to amorphous tapes, which results in a nanocrystalline structure. Nanocrystalline materials are characterised by improved loss and saturation properties.

1.4 Scope and outline of the thesis

The aim of this thesis is the analysis of inductive components for power electronics applications. Starting from the state of the art in inductor design, some newly developed considerations and approaches are proposed. A particular focus is reserved for inductors operating in DC-DC converters. As previously mentioned, core saturation is the main limit to design optimisation in this case. In addition, the core loss modelling is extremely critical due to the biasing effect of the DC current. The problem of the optimised design of inductors for DC-DC converters also faces the high-frequency operation of the windings, which can strongly influence the total losses of the component. Chapter 2 discusses the analysis of the test case of an output inductor for a buck converter to evaluate the multi-objective approach for maximising the power density and the efficiency of the component. A non-linear magnetic circuit model is adopted to compare the inductance profile of different design solutions, and the evaluation of the losses is performed through analytical formulations. The modelling of inductors for DC-DC converters is discussed, and some considerations are proposed on the most suitable approaches depending on the specific design requirements. In addition, the present work deals with the critical aspects of the multi-objective design, particularly the long computational time required. The multi-objective optimisation is approached with an artificial immune system based algorithm and enhanced with the adoption of a classifier system for

the constraint evaluation. In the design of inductors for DC-DC converters, the main time-consuming operation is the computation of the differential inductance profile for a given configuration. This evaluation involves time-consuming computational methods since it is related to the solution of a non-linear magnetic problem. In addition, the majority of the evaluated design configurations are unfeasible. An alternative to the conventional feasibility check is proposed by adopting a surrogate modelling approach. A classification system is proposed to evaluate the constraint of the configurations examined in the multi-objective optimisation process, highlighting interesting results in reducing the number of the required time-consuming computational tasks.

While some applications require a custom design of magnetic components, power electronic devices destined for mass production generally require commercially available components. In this case, the goals of high power density and high efficiency are reached by appropriately selecting the optimised part in the manufacturer catalogues. The conventional sizing approach of inductors for DC-DC converters aims to ensure the operation of the device in linear and stable conditions, overestimating the required inductance value and thus selecting an oversized magnetic component. It is well known that the operation of inductors for DC-DC converter is admissible even in partial saturating conditions, assuming the knowledge and the appropriate modelling of the component behaviour is provided. The operation of inductors in partial saturation reduces the size of an inductor for a given inductance value, increasing the power density of a DC-DC converter. However, inductors operating in partial saturation require appropriate modelling that considers the non-linearity introduced by ferromagnetic material behaviour. To this end, Chapter 3 describes a method for the experimental identification of the differential inductance profile of commercial ferrite inductors, also considering the effect of the overheating caused by the operative power losses. A setup based on a commercial DC-DC converter is proposed to perform the experimental characterisation, and an effective identification procedure is discussed. In addition, the modelling of the differential inductance profile is evaluated, and a methodology for the fast simulation of the current and voltage waveforms when the inductor operates in non-linear conditions is proposed.

The proper modelling of magnetic device properties can also be used to implement interesting control strategies for different energy conversion devices. In particular, Chapter 4 analyse the magnetic control of resonant converters, focusing on Wireless Power Transfer systems. The proposed magnetic control strategy is

implemented through a controlled variable inductor. The analytical modelling of a controlled variable inductor is described, defining the most suitable configuration to obtain the required differential inductance profile. The design is verified with finite element and circuit simulations, and a prototype of the controlled variable inductor is realised and tested. The controlled variable inductor is applied to an experimental Inductive Wireless Power Transfer system to verify the effectiveness of the magnetic control strategy. The regulation and supply system of the inductance value is also analysed. Adopting a controlled variable inductor is also proposed for a Capacitive Wireless Power Transfer system.

Chapter 5 reports some discussions and conclusions on the presented activities, in addition to considerations on future developments in the described topics.

1.5 List of publications

This thesis is partially based on the activities already presented in the following list of published and accepted papers in journals and conference proceedings:

1. L. Solimene, C. Ragusa, S. Musumeci, O. de la Barrière, and F. Fiorillo, '*Modeling of Saturable Inductors for Application in DC-DC Converters*', in 2019 26th IEEE International Conference on Electronics, Circuits and Systems (ICECS), Nov. 2019, pp. 839–842. doi: 10.1109/ICECS46596.2019.8964948.

2. C. Ragusa et al., '*Computation of current waveform in ferrite power inductors for application in buck-type converters*', Journal of Magnetism and Magnetic Materials, vol. 502, p. 166458, May 2020, doi: 10.1016/j.jmmm.2020.166458.

3. S. Musumeci, L. Solimene, C. Ragusa, M. Palma, and O. de la Barriere, '*Saturable Inductor Modelling in GaN FETs Based Synchronous Buck Converter*', in 2020 International Symposium on Power Electronics, Electrical Drives, Automation and Motion (SPEEDAM), Jun. 2020, pp. 396–401. doi: 10.1109/SPEEDAM48782.2020.9161961.

4. L. Solimene, S. Musumeci, and C. Ragusa, '*Saturable Ferrite Inductor Parameters Obtained Through a Double Step Optimization*', in 2020 55th International Universities Power Engineering Conference (UPEC), Sep. 2020, pp. 1–6. doi: 10.1109/UPEC49904.2020.9209887.

5. S. Musumeci, L. Solimene, and C. Ragusa, '*Identification of DC Thermal Steady-State Differential Inductance of Ferrite Power Inductors*', Energies, vol. 14, no. 13, p. 3854, Jan. 2021, doi: 10.3390/en14133854.

6. L. Solimene, F. Corti, S. Musumeci, C. Ragusa, and A. Reatti, '*Magnetic Control of LCC-S Compensated Wireless Power Transfer System*', in 2022 International Symposium on Power Electronics, Electrical Drives, Automation and Motion (SPEEDAM), Sorrento, Italy, Jun. 2022, pp. 160–165. doi: 10.1109/SPEEDAM53979.2022.9842241.

7. L. Solimene, F. Corti, S. Musumeci, A. Reatti, and C. Ragusa, '*Extended ZVS/ZCS operation of Class-E Inverter for Capacitive Wireless Power Transfer*', in 2022 IEEE International Conference on Environment and Electrical Engineering (EEEIC), Prague, Czech Republic, Jun. 2022, pp. 1–6. doi: 10.1109/EEEIC/ICPSEurope54979.2022.9854655.

8. L. Solimene, C. Ragusa and S. Musumeci, '*The role of materials in the optimal design of magnetic components for DC-DC converters*', Journal of Magnetism and Magnetic Materials (2022), vol. 564, p. 170038, Dec. 2022, doi: 10.1016/j.jmmm.2022.170038.

9. L. Solimene, F. Corti, S. Musumeci, C. Ragusa, A. Reatti, and E. Cardelli, '*Design and modelling of a controlled saturable inductor for an LCC-S compensated WPT system*', Journal of Magnetism and Magnetic Materials, vol. 564, p. 170056, Dec. 2022, doi: 10.1016/j.jmmm.2022.170056.

Other published papers on related topics are:

1. A. Canova, F. Freschi, L. Giaccone, M. Repetto, and L. Solimene, '*Identification of Material Properties and Optimal Design of Magnetically Shielded Rooms*', Magnetochemistry, vol. 7, no. 2, Art. no. 2, Feb. 2021, doi: 10.3390/magnetochemistry7020023.

2. S. Musumeci, C. Ragusa, M. Palma, and L. Solimene, '*Low-Voltage GaN FET in High Power Density Half-Bridge LED Driver*', in 2021 AEIT International Annual Conference (AEIT), Oct. 2021, pp. 1–6.
doi: 10.23919/AEIT53387.2021.9626936.

3. V. Barba, L. Solimene, M. Palma, S. Musumeci, C. Ragusa, and R. Bojoi, '*Modelling and Experimental Validation of GaN Based Power Converter for LED Driver*', in 2022 IEEE International Conference on Environment and Electrical Engineering (EEEIC), Prague, Czech Republic, Jun. 2022, pp. 1–6. doi: 10.1109/EEEIC/ICPSEurope54979.2022.9854660.

Chapter 2

Optimal design of inductive components

The ever-increasing demand for high power density converters requires the efficient design of magnetics since they significantly contribute to the device's dimensions, weight and losses. However, the loss reduction and the volume minimisation of magnetic components are challenging goals. The design problem is complex since different phenomena are strictly related. The current in the inductor determines the size of the conductors due to thermal-related problems, in addition to the size of the core, the number of turns, and the air gap length that influences the saturation of the core. The design of magnetic components for power electronics often requires a multi-objective approach [4, 5]. An approach that aims to reduce the losses should accept non-negligible core volumes, while a solution that reduces the volume leads to higher losses and over-temperature. For every multi-objective problem, an optimal design procedure can only define a set of solutions that belongs to the Pareto front, while the desirable configuration selection is assigned to the designer's needs. However, some considerations can be made to define the minimum loss solution for every available core volume.

In particular, in the first part of the following chapter, some considerations are presented on the design of the output inductor of DC-DC buck converters. The second part of the chapter is devoted to the multi-objective optimisation approach in the design of inductors for DC-DC converters, proposing a classifier approach for a fast evaluation of the problem's constraints.

2.1 The design of the output inductors for DC-DC buck converter

An output inductor of a DC-DC buck converter has to ensure an acceptable current ripple in all the current range of the application, combining low losses to ensure a high conversion efficiency. The output inductor of a DC-DC buck converter represents an interesting and challenging design problem. The operation of this component is related to high-frequency voltage waveforms with high ΔV between the ON and the OFF state, which strongly contribute to the losses of the magnetic core, and high average current that implies the saturation of the core, in addition to a further loss increase, both in the core and in the winding. The non-linear magnetic model of the inductor must be considered to ensure a differential inductance profile that guarantees an acceptable current ripple. In addition, the trade-off between power losses and core miniaturisation has to be faced, also considering the over temperature caused during the operation of the converter. The adopted methodology aims to compare the design configurations that guarantee a minimum inductance value required to limit the current ripple to a maximum prescribed value. This inductance value, defined as operative inductance, can be computed as

$$L_{\mathrm{op}} \geq \frac{(V_{\mathrm{IN}} - V_{\mathrm{OUT}})\, D}{\Delta I_{\mathrm{L}}\, f_{\mathrm{SW}}}, \tag{2.1}$$

where V_{IN} and V_{OUT} are the input and the output voltage of the DC-DC converter, D is the duty cycle, f_{SW} is the switching frequency, and ΔI_{L} is the current ripple at the prescribed output current. A triangular current ripple waveform is assumed to evaluate the operative inductance. The inductance profile comparison for design configurations can be made with the equivalent reluctance model of the magnetic component [6], represented by the series of an equivalent ferromagnetic path and an air gap path, whose reluctance is

$$\mathscr{R}_{\mathrm{fe}} = \frac{l_{\mathrm{fe}}}{\mu_0\, \mu_{\mathrm{fe,d}}\, S_{\mathrm{fe}}} \tag{2.2}$$

and an air gap path reluctance, defined as

$$\mathscr{R}_{\mathrm{gap}} = \frac{l_{\mathrm{gap}}}{\mu_0\, S_{\mathrm{gap}}}. \tag{2.3}$$

l_{fe}, l_{gap}, S_{fe} and S_{gap} are the ferromagnetic and air path length and cross-section, respectively, while $\mu_{\text{fe,d}}$ is the differential permeability of the core material. The equivalent total reluctance of the core is

$$\mathscr{R}_{\text{tot}} = \mathscr{R}_{\text{fe}} + \mathscr{R}_{\text{gap}} \tag{2.4}$$

and the differential inductance is defined as

$$L = \frac{N^2}{\mathscr{R}_{\text{tot}}}, \tag{2.5}$$

where N is the number of turns of the winding. To compute the differential inductance of the core, the differential permeability profile of the ferromagnetic material ($\mu_{\text{fe,d}}$) is required. The differential permeability is a function of the magnetic field strength that depends on the magnetomotive force applied by the winding. Thus, the equation

$$NI = H_{\text{fe}}\, l_{\text{fe}} + H_{\text{gap}}\, l_{\text{gap}} \tag{2.6}$$

has to be solved to find the relation between NI and H_{fe}. The polarisation fixed point (FP) technique is adopted to handle the non-linearity introduced by the ferromagnetic material [7]. A detail of the proposed methodology is reported in Appendix A.
Once the $H_{\text{fe}}(NI)$ relation is determined for a given geometrical configuration, the differential permeability profile $\mu_{\text{fe}}(NI)$ is computed, and adopted to evaluate the ferromagnetic path reluctance profile as a function of the output current of the converter. Figure 2.1 shows the comparison of two feasible differential inductance profiles for a given operating inductance value, one operating in linear conditions and the other operating in partial saturation. Adopting a non-linear model is required since the design configuration operating in partial saturation allows for further reduction of the core dimension, accepting a limited increase in the total losses [8, 9]. Figure 2.2 represents the design configurations obtained considering only the operation in linear conditions, compared to the ones achievable considering the operation partial saturation. As shown, the operation in partial saturation allows the exploitation of smaller core volumes, which would not result in feasible configurations considering only the linear operation.

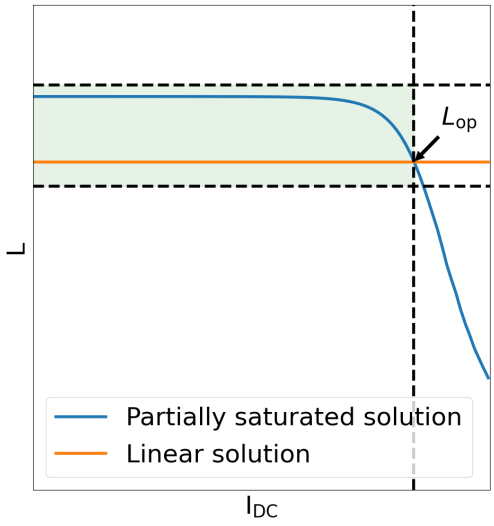

Fig. 2.1 Comparison of two design configurations, operating in partial saturation and in linear condition. The green box highlights the feasible operating inductance range.

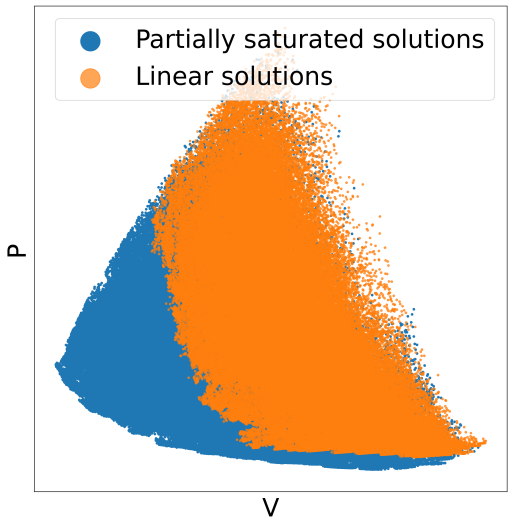

Fig. 2.2 Qualitative comparison of the solutions evaluated considering the operation in linear and in partial saturation conditions, in the space of the total losses and the core volume. The maximum magnetic flux density considered for the linear operation is 0.2 T

Thus, some partially saturated configurations could be part of the Pareto Front. As can be identified in (2.2), (2.3), (2.5), the design parameters that allow obtaining the suitable inductance value are geometrical (l_{fe}, l_{gap}, S_{fe}, S_{gap}), of the material (μ_{fe}), and of the winding (N). Once the method to evaluate the differential inductance profile is defined, the two objectives of the optimisation have to be evaluated for the

admissible configurations. The core volume is easily determined by the geometrical dimensions of the core, while the total losses of an output inductor for a DC-DC buck converter are defined as

$$P_{\text{tot}} = P_{\text{w}} + P_{\text{c}}, \tag{2.7}$$

where P_{w} represents the winding losses and P_{c} the core losses. The winding losses can be separetd in DC and AC losses. The DC winding losses can be defined as

$$P_{\text{w,DC}} = R_{\text{DC}} I_{\text{L}}^2. \tag{2.8}$$

R_{DC} is the winding resistance, determined by

$$R_{\text{DC}} = \frac{\rho \; l_{\text{w}} N^2}{S_{\text{w}}}, \tag{2.9}$$

where ρ is the copper resistivity, l_{w} is the mean length of the turn, and S_{w} is the window area available for the winding. The effective wire section, defined as $S_{\text{cu}} = S_{\text{w}}/N$, has to be adequately selected to guarantee an admissible current density in the wire. The mean length of the turns is related to the dimensions of the core's column where the winding is placed. The AC winding losses are caused by the high-frequency current ripple, and can be computed as

$$P_{\text{w,AC}} = R_{\text{AC}} \; I_{\text{L,}AC}^2. \tag{2.10}$$

where $I_{\text{L,}AC}$ is the RMS value of the current ripple and R_{AC} is the AC resistance of the winding, which can be considerably higher than the DC resistance, due to the non-homogeneous current density distribution at high frequency caused by skin and proximity effect. The ratio of $R_{\text{AC}}/R_{\text{DC}}$ reaches high values, up to 20, depending on the operative switching frequency. Thus, the increasing winding resistivity at high frequency is a non-negligible phenomenon, particularly for gapped core solutions. The air gap strongly influences the magnetic field distribution, determining a current density concentration in the near turns. In addition, the AC resistance value cannot be effectively estimated during the early design phase, requiring the knowledge of the conductors' location and the magnetic field distribution in the winding region. However, for a high current DC-DC output inductor, the $\Delta I_{\text{L,}\%}$ (peak to peak) generally does not exceed the 30% of the maximum average output current value. Considering a triangular current ripple waveform, the $I_{\text{L,DC}}^2/I_{\text{L,AC}}^2$ is

133.33. Considering $R_{AC}/R_{DC} = 20$, the AC winding losses determine an increase of 15% of the total winding losses. Moreover, some constructive tips, such as adopting a proper litz wire for the winding, help to reduce the R_{AC}/R_{DC} ratio [10]. Following these considerations, the AC winding losses are neglected to evaluate the optimised design of an output inductor for a DC/DC buck converter. An additional loss term is represented by the core losses, whose estimation can be performed with the Steinmetz Equation:

$$P_C = Vol_{fe}\, k\, f^{\alpha}\, \Delta B_p^{\beta}, \tag{2.11}$$

where ΔB_p is the peak magnetic flux density swing, defined as

$$\Delta B_p = \frac{0.5\,(V_{IN} - V_{OUT})\,D}{N\,S_{fe}\,f_{SW}}. \tag{2.12}$$

The Steinmetz equation is defined for sinusoidal flux density waveforms. The improved Generalized Steinmetz Equation (iGSE) allows computing the core losses under an arbitrary waveform, as [11] :

$$P_C = Vol_{fe}\,\frac{1}{T}\int_0^T k_i \left|\frac{dB}{dt}\right|^{\alpha} \Delta B_{pp}^{\beta-\alpha}\, dt, \tag{2.13}$$

where

$$k_i = \frac{k}{(2\pi)^{\alpha-1}\,\int_0^{2\pi} |\cos\theta|^{\alpha}\, 2^{\beta-\alpha}\, d\theta} \tag{2.14}$$

and ΔB_{pp} is the peak to peak magnetic flux density swing. Since the magnetic flux density waveforms applied by the DC-DC buck converter are triangular, the iGSE is adopted to evaluate the core losses. In addition, the inductor is under a high DC current that determines a DC magnetic field in the core material. The literature clearly states that a DC bias involves an increase in the magnetic losses and that the effect of the premagnetisation is variable for different magnetic materials. The parameters of the Steinmetz equation can be adjusted as a function of the applied premagnetising field H_{DC} [12]. However, the dependence of the parameters on the DC bias field has to be investigated with experimental measurements at different frequencies, magnetic flux density, and premagnetising field values. In addition, these parameters are generally not reported by the material's manufacturer. This lack of information forces the designer to neglect the effect of the DC bias on the core loss increase, knowing that the computed value will surely be underestimated. Thus, to compute the core losses with the iGSE, the k, α, β parameters provided

by the material datasheet are adopted [11, 13]. A further requirement for an output inductor of a DC-DC buck converter is the controlled over-temperature during regular operation. The appropriate estimation of the inductor heating requires also knowing the positioning of the other components on the PCB of the converter, and the thermal specifications of the surrounding materials, to implement a thermal finite element simulation. However, a preliminary estimation of the temperature rise caused by the inductor losses can be done considering a natural convection heat transfer condition, with a uniform heat flux density over the outer surface of the core exposed to air S_{T}:

$$\Delta T = \frac{P_{\mathrm{tot}}}{S_{\mathrm{T}} h_{\mathrm{c}}}. \tag{2.15}$$

The heat transfer coefficient is generally considered equal to $h_{\mathrm{c}} = 10\ \mathrm{W}/(\mathrm{m}^2\mathrm{K})$.

2.2 Preliminary analysis

The aim of this section is to provide some practical considerations on the comparison of different materials and different core, winding and air gap configurations. To this end, a case study is evaluated, whose specification are reported in Table 2.1

Table 2.1 Specification of the DC-DC converter.

Input voltage	48 V
Output voltage	24 V
Output current	10 A
Maximum current ripple (pp)	30 %
Switching frequency range	50 kHz $-$ 250 kHz
Inductance value range	80 μH $-$ 16 μH

Mn-Zn ferrite cores are the most adopted solutions for this kind of application. They are operated in gapped configurations to avoid the deep saturation of the inductor. The Mn-Zn ferrite, in fact, exhibits a low saturation flux density and a sharp differential permeability profile. On the other hand, metal powder cores are characterised by the "distributed" air gap property, which gives them effective permeability values similar to the gapped ferrite cores. In addition, the differential

permeability profile of this material is smoother even if compared to gapped ferrites. Thus, metal powder cores can be adopted to design un-gapped inductors. Another suitable choice can be represented by iron-based amorphous materials that show relative permeability and saturation flux density higher than ferrites, also combining competitive specific loss properties [14, 15]. For the presented case study, the N87 ferrite, the Xflux60 silicon iron powder and the Metglas 2605 SA-1 iron-based amorphous are considered. In order to compare the different materials, the same geometries are evaluated. In particular, Double E cores are considered. The E 8,8/2 core [16] represents the smaller core configuration, and the dimensions are then increased considering a linear scaling law for all the lengths, a quadratic one for the sections, and a cubic one for the volumes. The switching frequency is not considered as a given data but is a further degree of freedom of the design. The specifications are given in terms of the maximum ripple on the output current of the converter. Thus, following (2.1), the selection of a higher switching frequency allows for reducing the inductance value to control the current ripple, modifying the design requirement. Some comparisons of design performed considering different switching frequencies are proposed in the following. Given the core volume and the switching frequency, the design variables are the number of turns and the air gap length, which strongly influence the differential inductance profile and the total losses of the inductor. A comparison of all the admissible air gap - turns combinations is proposed in Figure 2.3 for the N87 ferrite, considering a switching frequency of 50 kHz.

For each core dimension, a minimum loss configuration can be identified. The lower loss configurations are characterised by larger core volume, while the lowest volume configuration has to face higher losses and even higher over-temperature due to the reduced surface available for heat exchange. Figure 2.4 represents the minimum loss solutions for each core dimension, considering a switching frequency range from 50 kHz to 250 kHz. The figure highlights that, in the considered range, a higher switching frequency allows for obtaining a design configuration with lower losses for a given core volume. This result can be motivated by the reduction of the inductance value required to keep the current ripple at acceptable values, which implies a lower number of turns for a given core geometry. The reduction of the number of turns determines lower DC winding losses, as reported in (2.8). In addition, as reported in (2.12), a higher switching frequency reduces the magnetic flux density swing, given the input and output voltages of the converter. However, the dependence of the core losses on the switching frequency should be further

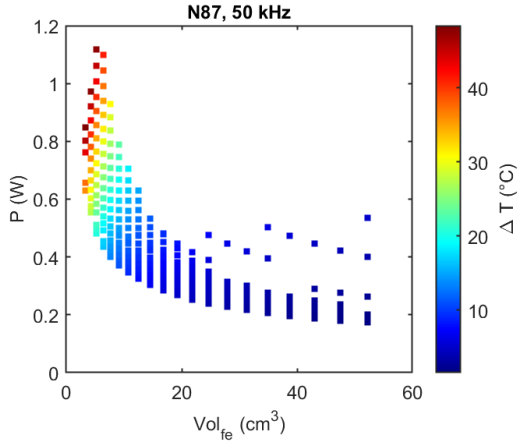

Fig. 2.3 Permissible solutions for the N87 ferrite at $f_{sw} = 50$ kHz. The plot compare the total losses and the volume of the core material. The colour bar represents the estimated temperature rise reached by each configuration.

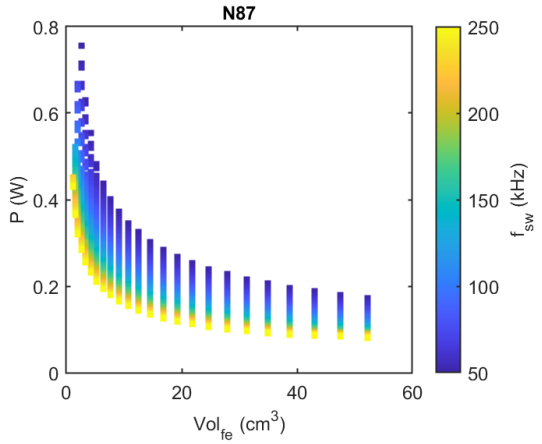

Fig. 2.4 Minimum losses solutions solutions for an N87 ferrite inductor, for each considered core volume. The plots compare the total losses and the volume of the core material. The colour bar represents the switching frequency considered for each configuration.

investigated. The effect of the reduced number of turns should be investigated, which implies a peak magnetic flux density increase. In addition, the relations of the α and β coefficients also have an influence, depending on the specific material properties. In addition, a higher switching frequency allows for using smaller core dimensions that do not guarantee admissible inductance values for the lower ones.

Figure 2.5 describes some specific design configurations, highlighting for each one the configuration that ensures the minimum losses. The winding, core and total losses are reported as a function of the permissible number of turns, and the permissible air gap lengths are also reported. In particular, Figure 2.5a represent a

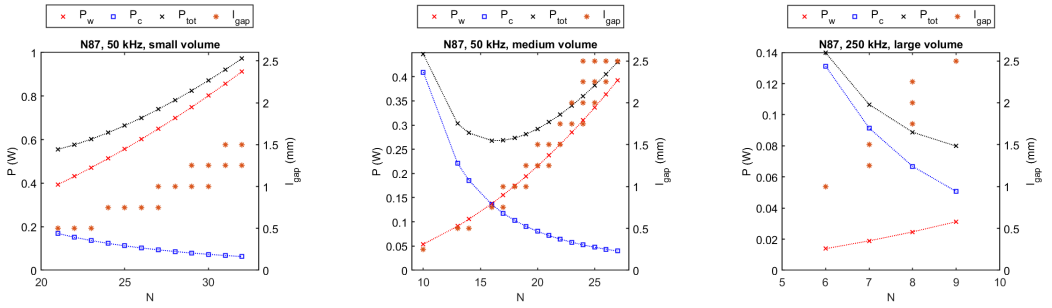

(a) (b) (c)

Fig. 2.5 Comparison of the different loss components, as a function of the selected number of turns, for different core dimensions and switching frequency values. The permissible air gap values for the reported configuration are also represented.

design solution for $f_{sw} = 50$ kHz, realised with a small core volume. In this case, a high number of turns are required to obtain the specified operating inductance value. Following (2.8), (2.12), (2.13), a high number of turns involves higher winding losses that increase with N, and lower core losses that decrease with N. Thus, the minimum loss configuration is represented by the configuration with the minimum admissible number of turns. Figure 2.5b shows the loss behaviour for a core of medium dimensions, with a switching frequency of $f_{sw} = 50$ kHz. Given the larger core dimensions, a lower number of turns is required; thus, the winding and core loss values are comparable. In this case, the minimum loss configuration is obtained when the balance of the two loss terms is achieved. The last case, reported in Figure 2.5c, is referred to a large core volume and a switching frequency of $f_{sw} = 250$ kHz. The higher switching frequency, which implies a smaller inductance value needed, and the larger core, which requires a reduced number of turns, decrease the effect of the winding losses on the total loss balance. The solution with the highest number of turns represents the minimum loss configuration since the core losses decrease as a function of N. As previously affirmed, the effect of the DC bias needs to be further addressed. However, some considerations can be stated. For small volumes, the relevant role of the winding losses, which can be further accentuated considering the AC term, tends to maintain the optimal configuration at the lower admissible number

of turns, even considering a severe increase in the core losses. At medium volumes, since the balance of two loss terms represents the minimum loss solution, higher core losses due to the effect of the premagnetisation determine an optimal number of turns higher than proposed in Figure 2.5b. In conclusion, for larger volumes, where the total losses are dominated by the core losses term, even considering the DC bias, the minimum loss configuration will be the one with the highest admissible number of turns. In all the presented cases, considering the DC bias effect, the total losses will be higher than proposed in Figure 2.5.
Concerning the adoption of different core materials, Figures 2.6a and 2.6b shows a comparison of the minimum losses configurations for the three considered choices, at $f_{sw} = 50$ kHz and $f_{sw} = 250$ kHz. The silicon iron powder material has the worst

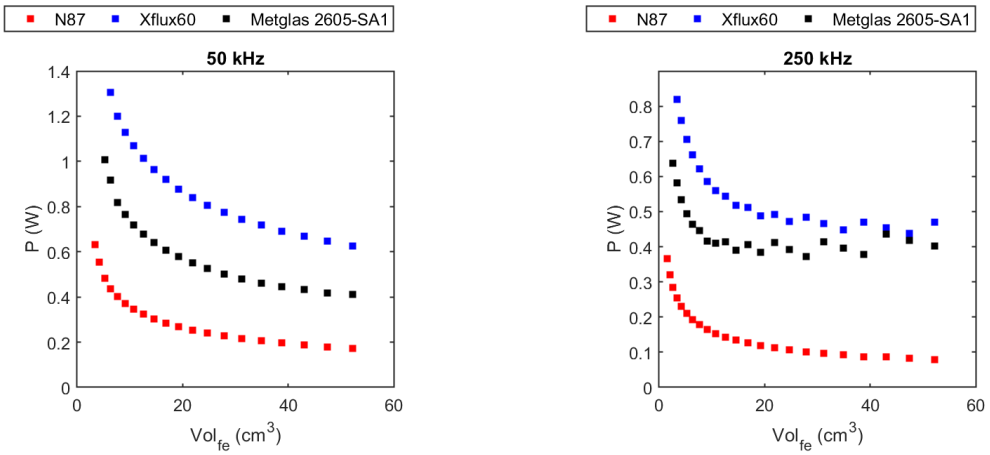

(a) (b)

Fig. 2.6 Minimum losses solutions for each considered core dimension, for the three analysed materials, at the minimum and maximum switching frequency. (a) 50 kHz. (b) 250 kHz.

performance in specific core losses, which determine the highest losses for each design configuration if compared with the other materials. The case study represented by the output inductor of a DC-DC buck converter does not exploit the low specific loss properties of the iron-based amorphous material well. In order to obtain the differential inductance profile in the entire current range required by the application, a high number of turn and air gap values are required, involving a strong influence of winding losses in the total loss balance. Compared with the analysed competitors, the N87 ferrite allows the minimum loss configurations. The relative permeability of this material is high, but the low saturation flux density makes adopting an air gap an unavoidable choice to achieve a smoother differential inductance profile requires the

addition of an air gap to avoid the deep saturation of the core. Due to the distributed air gap property, the silicon iron powder cores can be adopted even in un-gapped configurations. Figure 2.7 compares the differential inductance profile of a gapped ferrite solution and an un-gapped power core configuration.

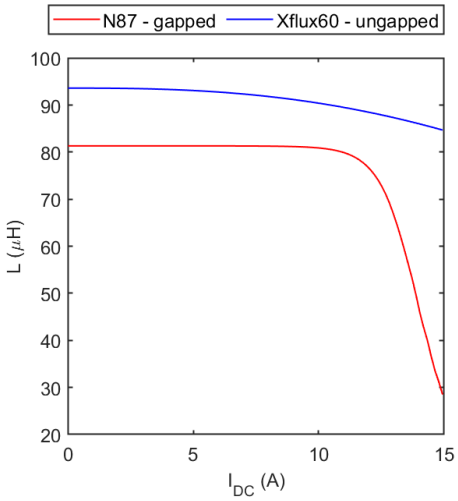

Fig. 2.7 Comparison of the differential inductance profile of a ferrite gapped configuration and a powder un-gapped configuration.

Even in the un-gapped configuration, the silicon iron powder cores exhibit a soft-saturating behaviour, smoother than ferrite, that can be desirable to ensure a higher stability of the current control of the DC/DC converter.

2.3 The role of the core material on the design output

Concerning the role of the different ferromagnetic materials adopted for the core, the analysis of the results indicates the influence their properties have on the optimisation of a DC-DC converter inductor design. Each material analysed has disadvantages that penalise achieving an optimal solution in terms of minimising losses and dimensions. However, the materials with high initial permeability, such as the ferrite and amorphous used, require the use of non-negligible air gap length to avoid deep saturation in the entire current range of the application. On the other hand, due to their distributed air gap property, silicon iron powder materials allow use in ungapped configurations but have worse specific loss properties leading to higher overall inductor losses. The ideal material for these applications would present a flat differential

permeability profile over a wide range of magnetic field values, thus avoiding a concentrated air gap or requiring a thin one. Furthermore, it combines this property with specific loss values comparable to or even better than those presented by ferrites, which are the standard for the realisation of inductors for DC-DC converters. For this purpose, the adoption of nanocrystalline materials could be helpful. It is known that the magnetic properties of these materials are controllable during the manufacturing process. Therefore, it would be possible to develop a material that, while not having high relative permeability values, operates in the linear region of the magnetisation characteristic up to sustained magnetic field values and combines excellent specific loss properties. There are currently commercially available materials that could fulfil these properties. However, the lack of information in the data sheets necessary for the designer to perform a preliminary design makes them unusable without an extensive experimental characterisation campaign to determine their essential specifications (differential permeability over a wide range of magnetic fields and specific loss as a function of switching frequency, magnetic flux density value and DC bias field).

2.4 Multi-objective optimisation

The design of an output inductor for a DC-DC converter is a multi-objective optimisation problem. In particular, as presented in 2.2, for a specific core size and a given switching frequency, a minimum loss configuration can be identified, defined by an adequately selected number of turns and air gap length configuration. As for every multi-objective optimisation problem, not a singular optimal solution is provided, but a set of solutions that belongs to the Pareto front. Selecting a configuration with low losses and a non-negligible size rather than one with a reduced size but augmented losses and operating temperature depends on the designer's specific requirements. Several algorithms have been proposed in the literature to face off the search of the Pareto front in a multi-objective problem, demonstrating various effectiveness and computational cost required for the convergence. However, a distinctive characteristic of all the multi-objective optimisation algorithms is the requirement of numerous objective function evaluations to find the Pareto front. Approaching the inductor design problem, the evaluation of the objective function requires the computation of the total losses and the component size, which are not particularly costly operations, if approached as in 2.1.

However, to ensure a feasible current ripple value, the differential inductance profile computation of each configuration must be evaluated. This computation requires at least the solution of the equivalent non-linear reluctance model proposed in 2.1 and computed with the iterative fixed point technique. However, for a more detailed approach, several magnetostatic finite element simulations could be required to evaluate the differential inductance profile over the entire current range of the DC-DC converter. The respect of a suitable differential inductance profile can be defined as a constraint of the optimisation problem, and its evaluation is more computationally expensive than the evaluation of the two optimisation objectives. In addition, for this kind of problem, the violation of the constraint on the differential inductance profile inevitably excludes a solution from the optimisation process. Thus, the evaluation of unfeasible solutions requires long unnecessary computational time. A viable approach to avoid the expensive evaluation of the inductance profile constraint can be represented by a surrogate model able to identify the feasibility of a configuration, not requiring the adoption of the iterative technique or finite element simulations. This approach consists of a classification process that aims to identify the design configurations corresponding to a feasible differential inductance profile among the large number of total configurations proposed during the evolution of the optimisation process. The classification task can be faced with several methodologies, from Artificial Neural Networks to Support Vector Machine techniques or Artificial Immune system-based classifiers. In this thesis, as a first attempt at the classification problem, the latter solution is implemented and tested for feasibility evaluation in the DC-DC output inductor design.

2.5 A classification strategy for feasibility evaluation

The analysis of the multi-objective optimisation approach to inductor design is performed on the simplified model described in 2.1. The selected geometry is the double-E core, and the adopted core material is the N87 ferrite. The specification of the evaluated case study are reported in Table 2.2

Table 2.2 Specification of the test case for multi-objective optimisation.

Input voltage	48 V
Output voltage	24 V
Output current	10 A
Maximum current ripple (pp)	30 %
Switching frequency range	50 kHz
Inductance value range	80 μH

The design variables, shown in Figure 2.8, are three geometrical dimensions of the core (A, B, F), the air gap length g, and the number of turns N. An assumption is made on the cross-section of the core: the cross-section of the central columns is two times the ones of the outer ferromagnetic paths.

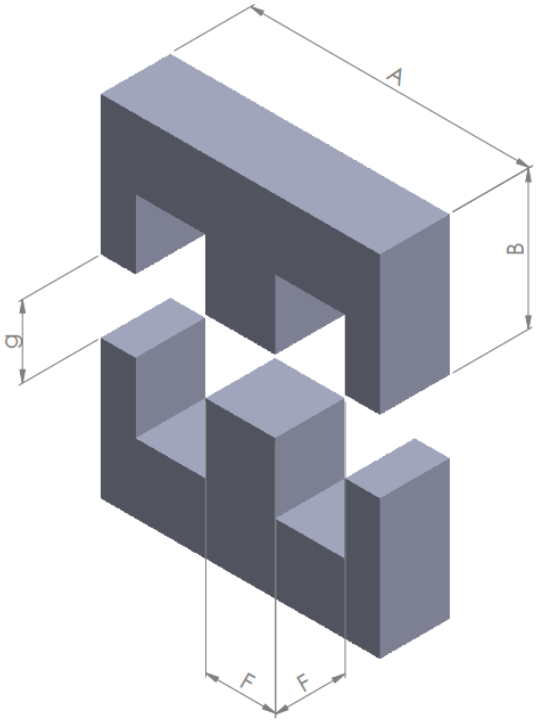

Fig. 2.8 Representation of the double-E core geometry. The considered variables for the optimisation problems are highlighted. A is the width of the E core. B is the height of the single E core. F is the dimension of the central column and g is the air gap length.

The considered range for the design variable is defined in Table 2.3:

Table 2.3 Range of the design variables

Variable	Lower bound	Upper bound
A	30 mm	59.2 mm
B	8 mm	22.3 mm
F	2 mm	8 mm
g	0 mm	2 mm
N	6	100

The optimisation objectives are the total losses of the inductor and the core volume, both to minimise. The constraints on the differential inductance profile are defined as follows:

$$L_{\text{min}} \leq L_{\text{op}} \leq L_{\text{max}} \ \wedge \ L_{\text{op}} \geq 0.6 \cdot L_0. \tag{2.16}$$

The first condition defines a bandwidth for the admissible inductance values that guarantee the current ripple limits. The second condition refers to the saturation of the inductor. As mentioned in 2.1, solutions that operate in partial saturation help to reduce the core dimension. However, an inductor that goes towards the deep saturation makes the current control critical and implies higher core losses due to the high DC bias magnetic field. A limit to the acceptable saturation rate is fixed with respect to the initial inductance value to avoid this issue. The constraints on the differential inductance profile are represented in Figure 2.9.

A further constraint is the maximum over-temperature the core can tolerate. Table 2.4 reports the considered constraint values.

Table 2.4 Optimisation contraints

Minimum inductance value	$0.95 \cdot L_{\text{nom}}$
Maximum inductance value	$1.2 \cdot L_{\text{nom}}$
Maximum ratio $L_{\text{op}}/L_{\text{in}}$	0.6
Maximum over-temperature	100 °C

The adopted multi-objective optimisation method is the Vector Immune System (VIS) proposed in [17]. This approach is based on implementing an artificial immune

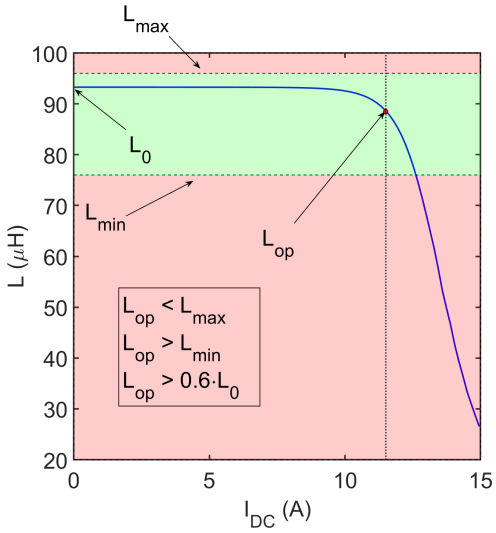

Fig. 2.9 Differential inductance profile of a design configuration as a function of the output current of the converter. The bandwidth of the admissible inductance value is highlighted in green. The proposed case represents a solution operating in partial saturation.

system that is intrinsically well-suited to multi-objective optimisation problems. The basic structure of the algorithm is developed as follows:

1. A randomly generated population of design configurations is created. Each design configuration is called cell. The constraint and objective functions evaluations are performed, and the fitness of each cell is evaluated. The randomly generated elements are called parents.

2. Each parent is replicated in N_{clones}, and each clone is locally mutated by random perturbation.

3. For each clone, the constraint and objective functions evaluations are performed, and the fitness is evaluated. The fitness is based on the Pareto dominance relations: if a cell is not dominated, its fitness is 1, while if everyone dominates it, its fitness is 0. The non-dominated cells between parents and clones are copied into memory.

4. For each parent and its clones, the cell with the best fitness is selected for the next generation (clonal selection).

5. Steps 2-4 are repeated N_{in} times and represent the inner loop.

6. The affinity of the memory cells is evaluated in the objective space, computing the Euclidean distance between them. A suppression method is applied to the memory cells whose distances are less than a threshold.

7. The surviving cells in the memory are copied into the initial population and new randomly generated individuals are added to them.

8. Steps 2-7 are repeated N_{out} times and represent the outer loop.

This method performs well compared to other well-established multi-objective optimisation methods, such as the widely adopted Non-dominated Sorting Genetic Algorithm II (NSGA-II) [18, 19].

Figure 2.10 represents the solutions of an optimisation execution for the proposed problem. The solutions are represented in the objective space, and the colours differentiate the feasible solutions and the unfeasible ones.

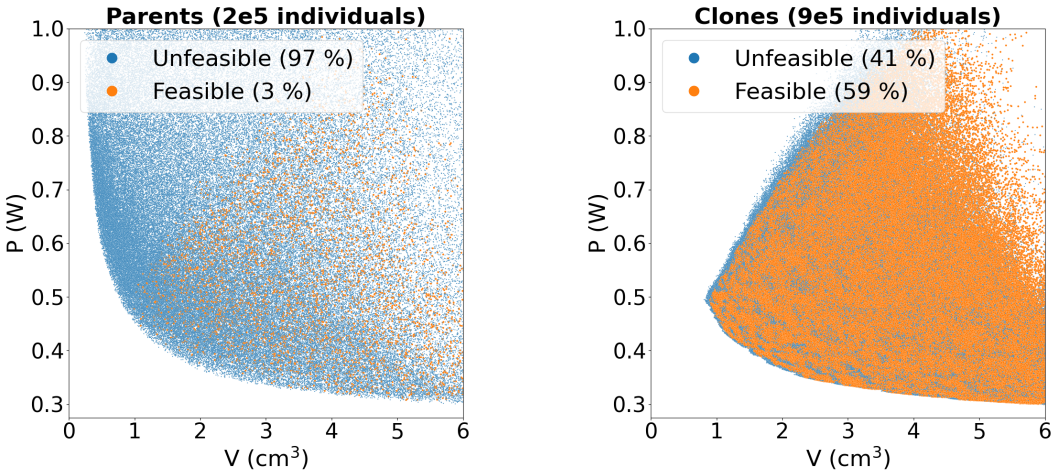

(a) (b)

Fig. 2.10 Representation of the feasible and unfeasible design configurations generated in an execution of the VIS optimisation. The orange dots represent the feasible solutions, while the blue ones are the unfeasible. The design configurations are reported in the design objective space, represented by the total losses and the core volume. (a) represents the randomly generated configurations (parents). (b) represents the locally mutated configurations (clones). The total number of evaluated parent and clones design is reported.

The analysis of the proposed output highlights that in the randomly generated cells (parents), only a limited percentage of them satisfy the constraint, as reported in Figure 2.10a. Since the unfeasible cells are disregarded, a considerable amount

of constraint evaluations could be avoided, saving computation time. Considering that the clones are locally mutated by parents that still satisfy the constraints, the higher percentage of feasible cells, shown in Figure 2.10b, is motivated. However, the number of clones is about five times the number of parent cells. Thus, in this case, many FP evaluations could be avoided. Considering all the evaluated cells, about 50% of the design configurations are unfeasible. More than 500000 FP computations could be avoided by adopting a surrogate model to predict the feasibility of a design configuration before its evaluation. A binary classification problem has to be faced from the considered surrogate model, which has to predict if a design configuration belongs to the feasible or the unfeasible set. Further considerations can be made by analysing the location of feasible and unfeasible solutions in the design variable space, as reported in Figure 2.11. In particular, the three variables adopted for the plot are the dimension of the central column F, the air gap length g, and the number of turns N, which mainly influence the design output. In Figure 2.11a, the orange

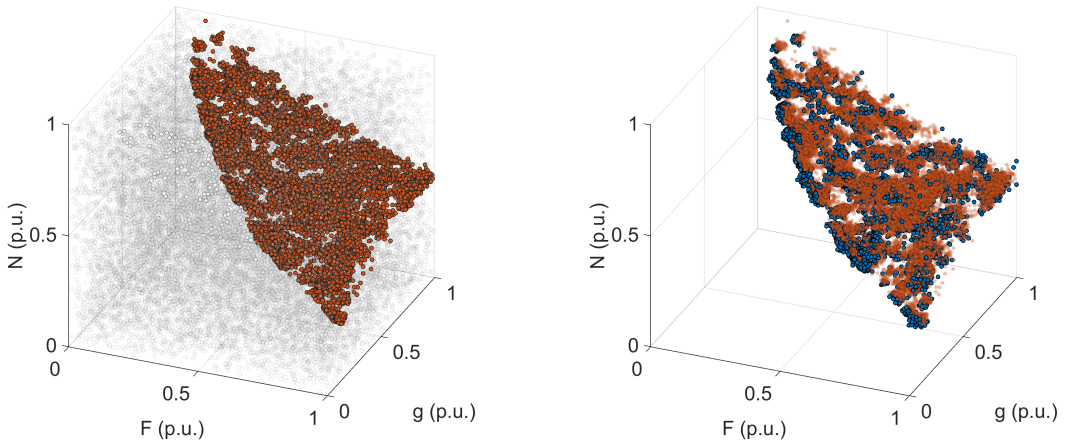

Fig. 2.11 Design configurations evaluated in a VIS optimisation execution. The solutions are represented in the design variable space determined by the number of turns, the dimension of the central column and the air gap length. (a) show in orange all the feasible configurations of the VIS executions, while in grey are reported the unfeasible randomly generated solutions. (b) describes in orange all the feasible configurations of the VIS executions, while the blue dots are the unfeasible solutions generated with local mutations.

point represents all the feasible solutions, while the grey points are the unfeasible solutions in the randomly generated cells. The plot highlights how there are, in the design variable space, some regions only populated by bad individuals that are easily recognisable. On the other hand, in Figure 2.11b is apparent how the unfeasible

cells, generated by local mutations and represented in blue, are shuffled in the region where the good solutions are located. In this case, the feasibility identification for a given configuration becomes more challenging.

2.6 Test of an Artificial Immune System based classifier

As previously mentioned, different approaches can be adopted to face the proposed binary classification problem. As a first attempt, the tested approach applies a classifier system based on an Artificial Immune System (AIS) [20]. This classifier is composed of memory cells, called antibodies (ABs), that are the recognition units for the configurations that have to be classified, defined as antigens (AGs). The final class of an AG is determined by combining the answers of the stimulated ABs. The choice of this classifier is motivated by the shared structure with the VIS since both are based on AISs. However, in future developments of this research activity, other approaches will be defined to solve the classification problem. Adopting the classifier in the optimisation process implies that each cell (parents and clones) has to be classified as feasible or unfeasible. The solutions classified as unfeasible are disregarded and not evaluated with the FP iterative method. The combination of the classifier-fixed point answers, summarised by the confusion matrix represented in Figure 2.12, are:

- True positives: feasible solutions classified as "positive". They must be evaluated in the optimisation process.
- False positives: the unfeasible solutions classified as positives. The incorrect classification of these combinations implies unnecessary evaluations through the FP iterative technique.
- True negatives: the negative classified solutions that are unfeasible, which can be correctly disregarded in the optimisation process.
- False negatives: the negative classified configurations that are instead feasible. These solutions are wrongly disregarded, representing the worst case since some design configurations that could belong to the Pareto Front are no more considered in the optimisation process.

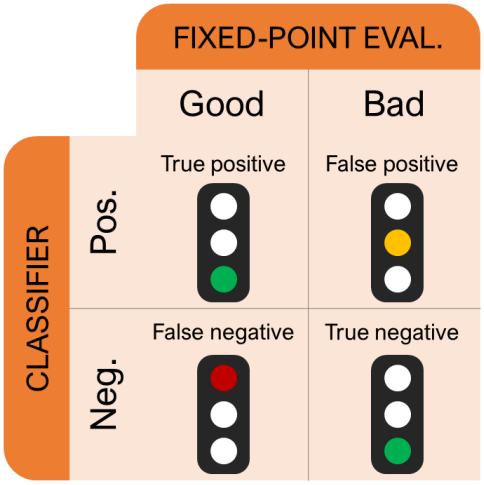

Fig. 2.12 Confusion matrix of the classification and the evaluation with the FP iterative technique. The traffic light symbol highlights the effect of the answer on the optimisation process: the green light represents a correct classification, the yellow light represents an incorrect evaluation that does not influence the optimisation output, and the red light represents an incorrect classification, which can negatively influence the optimisation execution.

The proposed AIS-based classifier system must be trained on a dataset of previously evaluated configurations to define the antibodies. The definition of the dataset is a critical task that can strongly influence the performance of the classifier system. For the proposed problem, a randomly generated database of configurations will be strongly unbalanced since most of them are unfeasible. Adopting an unbalanced dataset for the classifier training would lead to a weak accuracy of the feasibility evaluation. To this end, over 80000 randomly generated configurations, all the 2500 feasible solutions are selected, and the other 2500 unfeasible solutions are randomly extracted in the remaining configurations to form a balanced training/test dataset. The ratio of the training/test dataset is 0.8. The training of the AIS-based classifier is then performed. A run of optimisation with VIS is executed to evaluate the effectiveness of the trained classifier in the multi-objective optimisation process. For each cell, the feasibility evaluation is performed with the standard approach (FP method for the constraints on inductance profile) and the classification approach. Tables 2.5 shows the results for the parents and the clones.

Table 2.5 Classifier performances

	Parents	**Clones**
True positive (%)	44	67
False positive (%)	56	33
True negative (%)	99	51
False negative (%)	1	49
Total positive	$8e^3$	$500e^3$
Total negative	$200e^3$	$400e^3$

Some remarks can summarise the proposed results:

- As presented in Figure 2.10a, in the randomly generated individuals, the unfeasible solutions are the majority. The very high percentage of correctly classified negatives considerably reduces the number of FP evaluations. A high number of false positives classifications has to be noted. However, due to the low number of feasible configurations in parents, the unnecessary evaluations of the FP are negligible.
- The effective negative classification obtained in parents can be motivated by the location of the unfeasible configurations in the variable space, as previously presented in Figure 2.11a. In the space of the design variables, some regions containing exclusively unfeasible configurations can be identified. If well-trained, the effectiveness of the classification in this region is supposed to be high.
- As discussed when describing 2.11b, in the locally mutated solutions, the unfeasible regions are not well delimited, and the adopted classification of the negative elements is less effective. While the true negatives classification percentage allows for avoiding about 200000 FP evaluations, an equivalent number of feasible configurations are wrongly disregarded. The effect of this wrong classification will be visible when describing the Pareto quality indexes.
- The percentage of false positives on clones is reduced compared to parents. However, about 150000 configurations are unnecessarily evaluated.

The presented performance could be more satisfactory regarding the influence of the classifier on the quality of the obtained Pareto Front. However, the AIS-based classifier shows interesting performances in reducing FP evaluations. To further investigate these aspects, a comparison of the results for three different approaches is proposed:

- Execution of VIS optimisation method without a classifier (VIS).
- Application of the classifier only on randomly generated configurations (VIS_{AIS})
- Application of the classifier both on randomly generated and locally mutated configurations ($\text{VIS}_{\text{AIS,clone}}$).

For each of the presented cases, 20 optimisation executions are performed. The first result is the average number of FP evaluation calls, reported in Figure 2.13, in which separated results are reported for the classification of parents and clones.

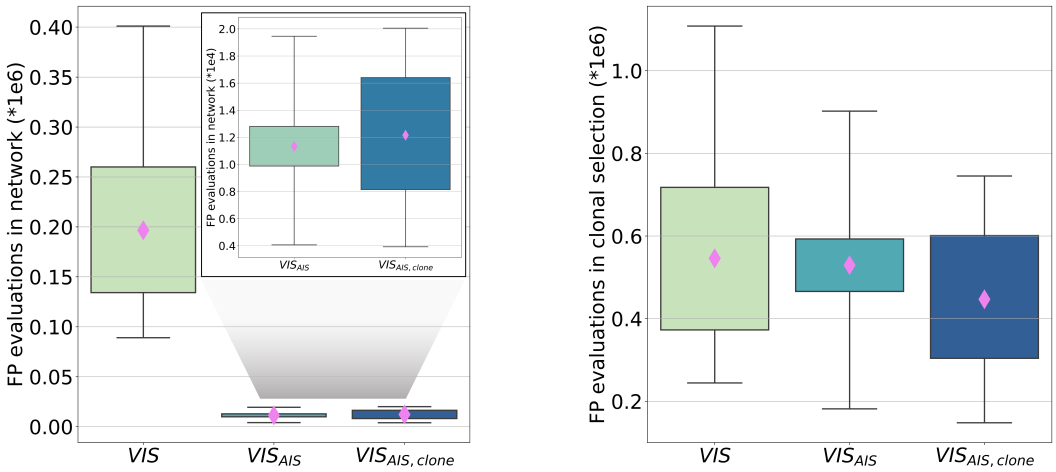

(a) (b)

Fig. 2.13 Box plots of the FP executions in the 20 runs of the three tested approaches. The pink diamonds represent the mean value of each case. (a) describes the FP evaluations for the randomly generated cells. A zoom of the results for the two classifier approach is reported in the upper right corner. (b) describes the FP evaluations for the locally mutated cells

When considering the FP evaluations related to the randomly generated elements, reported in Figure 2.13a there is a considerable advantage in adopting the classification. This result can be motivated on the basis of the previous observations on the distribution of the unfeasible randomly generated solutions in the design variable

space, which leads to a classification accuracy of 99% on true negative elements. In addition, the unfeasible solutions constitute the 97% of the parents generated in VIS optimisation, allowing a considerable FP evaluation saving. By observing Figure 2.13b, the adoption of the classification on clones allows to reduce the FP iterations, but this result can be further improved by reducing the bad recognition of unfeasible solutions. Figure 2.14 reports the total FP calls for the three cases.

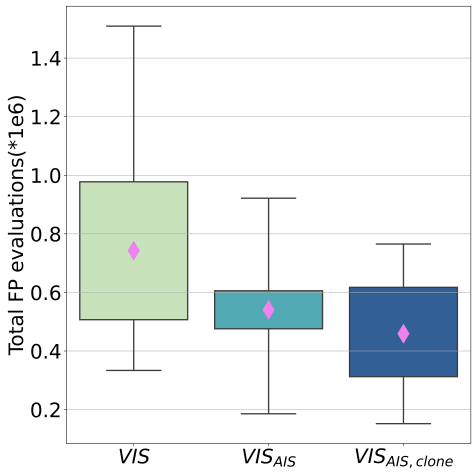

Fig. 2.14 Box plot of the total FP executions in the 20 runs of the three tested approaches. The pink diamonds represent the mean value of each case

Based on the preliminary considerations, about 50% of the configurations generated in the VIS optimisation are unfeasible, and thus a perfect classifier allows for avoiding, on average, 400000 FP calls. When applied only on parents, the tested classifier avoids 260000 calls, while when applied on parents and clones, it avoids about 400000 calls. These results are quite satisfactory but can still be improved by adopting a more effective classification system in the region of the locally mutated cells. Other considerations can be done by observing the Pareto Fronts obtained through the three proposed approaches, reported in Figure 2.15.

For a given approach, the proposed Pareto Front is defined by selecting the non-dominated solutions between the results of the 20 runs. In addition, the Pareto Front of the randomly generated configurations adopted for the training-test dataset of the classifier is reported. As shown, practically none of the configurations in the dataset belong to the true Pareto Front. A substantial overlapping of the three fronts can be observed, except for the region of the lowest volume cores. Clearly, in these regions, the constraint evaluations became more critical for two reasons:

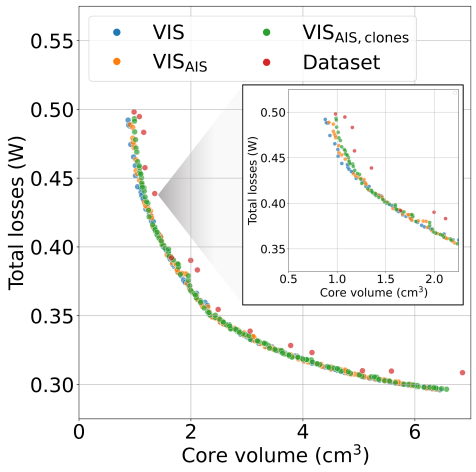

Fig. 2.15 Pareto fronts of the analysed design case, obtained with the three proposed approaches. The reported fronts are computed by combining the solutions of the 20 executions performed in each case. In addition, the Pareto front of the training-test dataset is reported. A zoom of the Pareto fronts in the region of small volumes is also reported to highlight the marked differences in this area.

the first is related to the core saturation, which is more likely to happen for small volume cores, which are attractive for the operation in partial saturation. The second is related to the maximum over temperature. A small core solution belonging to the Pareto Front is characterised by non-negligible total losses and a reduced outer surface for heat dissipation that can lead to exceeding the thermal limit fixed by the application specification. It is apparent from Figure 2.15 how the adoption of the classifier on parents and clones involves a worsening of the Pareto Front, which can be motivated by the high percentage of false negatives classifications in clones. As previously described, false negative configurations are wrongly disregarded in optimisation. The number of wrongly disregarded configurations is about 200000, and these may include design solutions belonging to the Pareto Front. The worsening of the Pareto Front can be analytically evaluated by considering some performance measurements. In particular, the Reverse Generational Distance (RGD) is evaluated. This performance index computes the distance d_i for each solution jth in the Pareto True to the closest solution in the Pareto known. The mean value over the True Front is then considered:

$$RGD = \frac{1}{N_{\text{true}}} \sqrt{\sum_{i=1}^{N_{\text{true}}} d_i^2}. \tag{2.17}$$

Since the Pareto True cannot be analytically evaluated for the presented case, the following assumption is made: the Pareto True is defined as the set of non-dominated solutions evaluated in all the 60 runs performed with the three different approaches. The other considered Pareto quality index is the Spacing (S), which measures how well the solutions of the Pareto Known are distributed. The Spacing is defined as:

$$S = \sqrt{\frac{1}{N_{\text{known}} - 1} \sum_{i=1}^{N_{\text{known}}} (\bar{d} - d_{\text{i}})^2} \tag{2.18}$$

where $\bar{d}$ is the mean value of all d_{i}.

Figure 2.16 shows the results for the two presented performance measures.

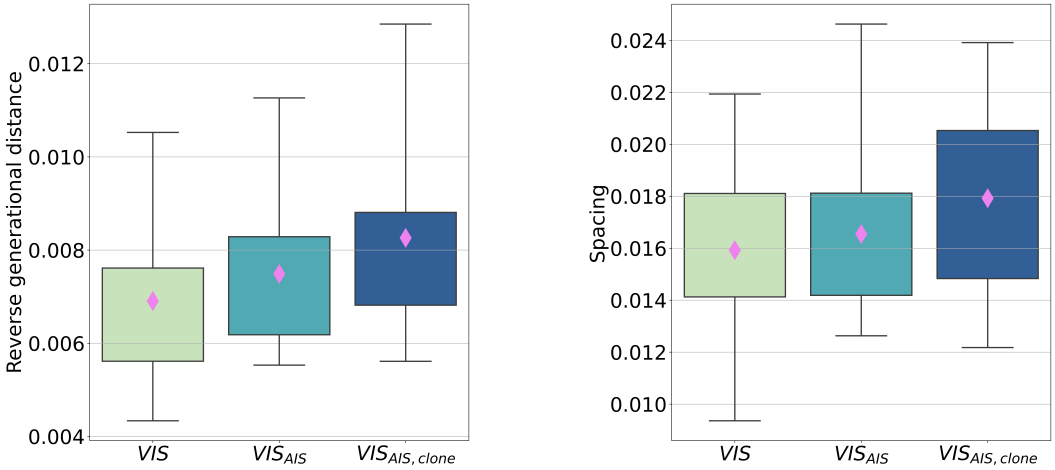

(a) (b)

Fig. 2.16 (a) Box plots of the reverse generational distance index for the 20 runs of the three tested approaches. The pink diamonds represent the mean value of each case. (b) Box plot of the spacing index for the 20 runs of the three tested approaches. The pink diamonds represent the mean value of each case.

A lower value for S and RGD is related to a better quality of the obtained Pareto Front. The Spacing is not particularly affected by the adoption of the classifier since it is mainly determined by the characteristic of the VIS methodology adopted. On the other side, the RGD shows a worsening that increases as the influence of the classification on the optimisation process increases. In particular, the worst behaviour is found with the adoption of the classifier on parents and clones. As seen before, the wrong classification of the small volume solutions determines a higher distance

of the Pareto Fronts obtained with this approach, with respect to the Pareto True that in this region is totally determined by the solutions obtained with the VIS method without classification on the constraint evaluation.

2.7 Discussion on the classification approach results

The adoption of a classification-based feasibility evaluation in the design of output inductors for DC-DC converters aims to reduce the number of time-consuming computations required by the conventional approach. In particular, the fixed point iterative technique is used for the proposed preliminary design to compute the differential inductance for each configuration. However, in a more detailed design approach, electromagnetic finite element simulations are adopted to evaluate the feasibility of a given differential inductance profile. It should be noted that, for the training of the classifier system, a non-negligible number of conventional feasibility evaluations is required to build up a consistent dataset. However, the computational effort required for the training is considerably lower than the one required in an optimisation execution. In addition, the classifier training can be generalised for optimisation problems related to different inductance constraints. If the non-linear computation is generalised to a given core geometry and air gap values, the equivalent reluctance profile can be obtained as a function of the applied magnetomotive force. The computed profile is not strictly related to a given inductance value since different numbers of turns allow to obtain different differential inductance profiles. From a single set of non-linear problem solutions, different training datasets for different inductance profile constraints can be obtained by relating the computed non-linear reluctance profile to the number of turn values admissible for the considered optimisation problem, further improving the computational efficiency of the proposed approach.

Furthermore, the convenience of the classification approach strongly depends on its effectiveness in feasibility evaluation accuracy. As the first attempt, an Artificial Immune System-based classifier has been selected. The obtained performances demonstrate the opportunity to considerably reduce the feasibility evaluation with conventional time-consuming approaches, still obtaining good results in the output of the optimisation process. The design of output inductors for DC-DC converters shows the presence of many unfeasible configurations in the design space, determining a

highly unbalanced dataset for the training of the classifier. In future developments of this research activity, other classification strategies will be explored to better deal with the unbalanced nature of the problem.

Chapter 3

Adoption of saturable inductors for DC-DC converters

The innovation in the field of semiconductor devices is pushing towards the miniaturisation of power converters, allowing high switching frequencies that ensure the converter's power density improvement. However, passive components, such as capacitors and inductors, represent the bottleneck to the miniaturisation of converters. In particular, inductors are some of the bulkiest components of a DC/DC converter board and are also responsible for a relevant amount of the weight of these devices. In contrast to the semiconductor sector, in recent years, only slight improvements have been reached in the magnetic material field, where the technologies seem to be more mature and consolidated. Thus, the improvement in the power density of magnetic components for power converters should be researched in the proper exploitation of the available magnetic materials. As presented in 2, magnetic components' design can also benefit from the switching frequency increase, which allows the adoption of cores with reduced volume. In the case of the inductors for DC-DC converters, however, the obstacle to the miniaturisation is represented by the saturation of the magnetic core [9]. In fact, the inductors operating in DC-DC converters structure are subjected to a magnetic field bias caused by the DC currents proper of these structures. The DC magnetic field bias leads to the operation of core materials towards the saturation region of the magnetisation curve. This condition implies that the differential permeability of the ferromagnetic material drops to values considerably lower than the initial one, causing a reduction of the differential inductance of the component. Usually, the converter's designers adopt

a conservative approach, considering the operations in the non-linear region of the magnetisation curve an undesirable condition. Due to avoiding inductor saturation, the standard design rules lead to oversized cores, which do not allow the proper exploitation of ferromagnetic material. On the other hand, adopting inductors operating in partial saturation allows for optimising the magnetic design, reducing the weight and volume of the components. The saturated operations of inductors for DC-DC converters are widely adopted for ferrite inductors [9, 8, 21]. Ferrites exhibit a sharp differential permeability profile and are typically operated in gapped core configurations to avoid the deep saturation of the realised inductors. However, even in gapped ferrite inductors, a sharp differential inductance profile is obtained that requires a suitable model to properly consider the non-linear behaviour of saturable inductors in DC-DC converters, in addition to a proper tool to evaluate the operating current and voltage waveforms. Due to the operation at non-negligible DC current values, the losses of ferrite inductors operating in saturation have to be taken into account, considering that a loss increase leads to a temperature increase that could deteriorate the magnetic properties of the core material, leading to higher losses. Thus, the differential inductance profile is also influenced by the operating temperature of the inductor. In the literature, different modelling and characterisation methods of saturable ferrite inductors are described, also taking into account the operating temperature variation [22–27]. The approaches that require the operating temperature measurements are not easily adoptable since the inductor temperature is critical to measure during the normal operating conditions of a power converter. Other approaches are based on the relation between the temperature and the power dissipation of the inductor, thus defining a loss-dependent inductance model that requires a set of experimental measurements under a wide range of operating current and loss conditions [28]. However, a saturable inductor for a DC-DC converter is frequently characterised by higher winding losses rather than core losses. As described in 2, in this case, the total losses of the inductor are strictly related to the average operating current of the component, and thus, the steady-state temperature of the inductor can be related only to the average current value. This assumption allows for defining a characterisation method of the differential inductance profile of ferrite inductors, considering the influence of the operating temperature on the magnetic material properties, requiring a limited set of experimental measurements at different average current values. The obtained characterisation can be used in the design and control systems of DC-DC converters operating with inductors in partial

saturation under a wide range of working conditions. This approach is presented in [29] and reported as the identification of the DC thermal steady-state of ferrite inductors.

3.1 The prevalent role of DC winding losses in saturable inductors

In an inductor for DC-DC converters, two loss terms can be identified, as mentioned in Chapter 2 . The first is represented by the core losses, a function of the ferromagnetic material properties, of the operating frequency and applied voltage waveform. Even the applied average current influences the core losses due to the DC bias magnetic field applied in the core material. However, even if it is known that the DC bias field increases the core losses of several magnetic materials, there are no precise experimental data or physical models to establish the dependence of these losses from the bias field. The second term is represented by the ohmic losses in the inductor winding. A share of the winding losses is related to the average current value and the DC resistance of the winding, while another term is dependent on the high-frequency increase of the winding resistance caused by skin and proximity effects and on the RMS value of the current ripple. As presented in Chapter 2, the DC winding losses frequently represent the prevailing effect in an inductor operating near saturated conditions. Tables 3.1 and 3.2 report the loss data available for some commercial inductors under different operating conditions.

Table 3.1 DC and AC losses for the Coilcraft MSS1260T-273, under different switching frequency and input voltage values. The considered output current is near the declared saturation current.

MSS1260T-273 ($I_{SAT} = 4.7$ A)					
V_{in} (V)	δ	f_{sw} (kHz)	I_{out} (A)	P_{DC} (mW)	P_{AC} (mW)
24	0.5	500	4	768	74
32	0.5	500	4	768	132
24	0.5	1000	4	768	31

Table 3.2 DC and AC losses for the Coilcraft SER1390-333, under different switching frequency and input voltage values. The considered output current is near the declared saturation current.

SER1390-333 ($I_{SAT} = 4.7$ A)					
V_{in} (V)	δ	f_{sw} (kHz)	I_{out} (A)	P_{DC} (mW)	P_{AC} (mW)
24	0.5	500	4	336	44
32	0.5	500	4	336	79
24	0.5	1000	4	336	34

It can be observed that even considering different switching frequencies and current ripple values, more than 80% of the total losses of inductors operating at average current close to the saturation values are constituted by the DC winding losses. In these conditions, it can be assumed that the over-temperature of the inductor is caused mainly by this loss term, defining a strict relation between the DC current and the steady-state temperature of the component. Since the DC current is an easily measurable quantity compared to the operating temperature of the ferromagnetic core, it can be helpful to define a differential inductance profile that relates the over-temperature effect caused by varying average output current values up to the saturation of the core.

3.2 Experimental setup for the differential inductance profile identification

The identification methodology is applied to commercial ferrite inductors. Generally, manufacturers do not provide information on the core material composition, the air gap length, or winding specifications. In addition, frequently, commercial inductors are shielded, and thus only the external leads are accessible for the measurements. The only measurable quantities are the inductor voltage and current waveform. The differential inductance profile is determined by adopting the experimental setup described in Figure 3.1. A synchronous buck converter derived by the evaluation board circuit EPC90122 is used since the GaN devices allow high switching frequency, up to 1MHz. An arbitrary waveform generator is used to regulate the switching

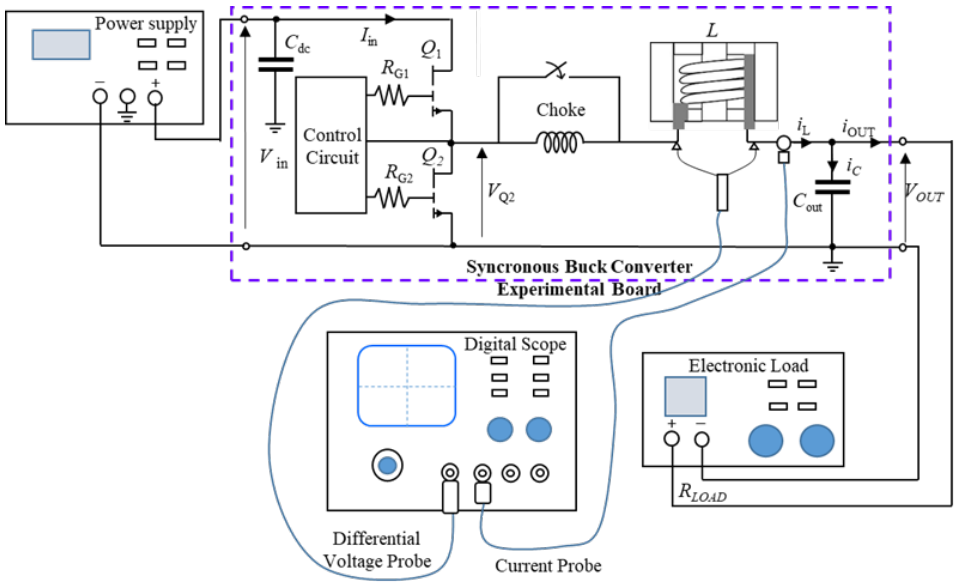

Fig. 3.1 Setup adopted for the identification of the differential inductance profile of commercial ferrite inductors. The voltage and current waveforms are regulated through the synchronous buck converter EPC90122. The output current is regulated with an electronic load. The inductor current and voltage waveforms are acquired with a digital oscilloscope.

frequency and the duty cycle of the converter. A regulated power supply controls the input voltage, while the output current is determined with an electronic load. Several operating conditions of the inductor can be tested with the proposed setup. Since the previously described assumption states that the steady-state operating temperature of a saturable inductor is mainly influenced by the average output current, in order to avoid the effect of the current ripple, a choke with high inductance and saturation current ($L = 600\ \mu$H and $I_{\mathrm{SAT}} = 150$ A) is inserted in series to the inductor under test. The high inductance value allows for the current ripple reduction to negligible values, making the AC losses of the inductor under test negligible. In this case, the steady-state temperature of the inductor is only related to the selected average output current value of the load. After reaching the thermal steady-state condition for a given DC current, the additional choke is short-circuited, and the inductor voltage and current waveforms are immediately measured, avoiding the variation of the component temperature. The measured quantities are acquired with a digital oscilloscope, a differential voltage probe and a current probe. The identification procedure is presented for the two inductors described in Tables 3.1 and 3.2 (Coilcraft MSS1260T-273 and SER1390-333). The manufacturer declares for the MSS1260T-273 inductor an initial inductance value $L_0 = 27\ \mu$H and a saturation current $I_{\mathrm{sat}} = 4.7$ A, while

for the SER1390-333 $L_0 = 33\ \mu$H and $I_{sat} = 4.8$ A. The manufacturer defines the saturation current as the current that causes a 30% inductance drop. These inductors have comparable initial inductance and saturation current and can be tested under the same operating conditions. However, as reported in the data sheets and shown in Figure 3.2, the over-temperature dependence on the average current for the two devices is significantly different due to different constructive characteristics, as shown in Figure 3.3.

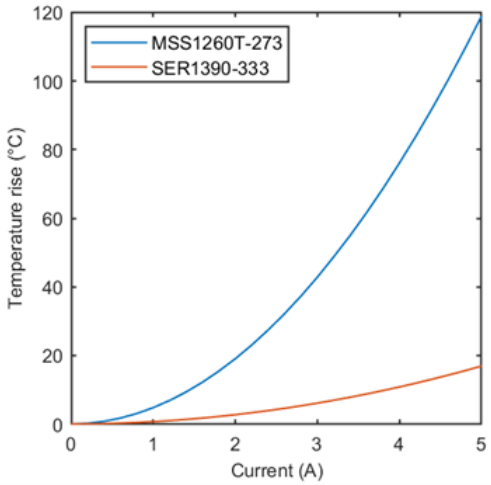

Fig. 3.2 Comparison of the temperature rise caused by increasing average output current for the Coilcraft MSS1260T-273 and the Coilcraft SER1390-333.

Fig. 3.3 Photo of the two tested inductors. The MSS1260T-273 is on the left, the SER1390-333 is on the right.

The identification procedure demonstrates to be effective for the different analysed cases.

3.3 Differential inductance identification procedure

The measured voltage waveform includes the voltage drop on the winding resistance, which is removed in order to obtain the inductive voltage:

$$v_{\mathrm{L}}(t) = v_{\mathrm{L,exp}}(t) - R_{\mathrm{s}} \cdot i_{\mathrm{L}}. \tag{3.1}$$

The flux linkage is computed as

$$\Phi(t) = \Phi(i_{\mathrm{L}}(0)) + \int_0^t v_{\mathrm{L}}(t')dt' \tag{3.2}$$

The computed flux linkage is defined minus a constant term representing its value at $t = 0$. Thus the obtained flux linkage waveform can be related to the experimental current waveform, determining a loop with a non-zero area due to the dissipative effects in the magnetic core [30]. However, if the measurement is performed with a duty cycle $\delta = 0.5$, the loop is symmetrical since the losses in the semi-period are equal, and the average $\Phi(i_{\mathrm{L}})$ is computed as the mean value between the two half loops. Figure 3.4 represents the $\Phi(i_{\mathrm{L}})$ relation for increasing average output current values.

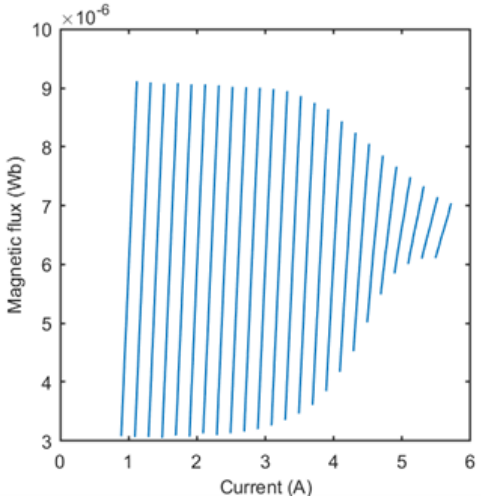

Fig. 3.4 Average $\Phi(i_{\mathrm{L}})$ curves for increasing average output currents, for the Coilcraft MSS1260T-273. The represented magnetic flux swing is limited to the linear behaviour for each average output current.

For each tested DC current, an appropriate current sweep amplitude for which the characteristic is linear can be identified. In this interval, the differential inductance

value is identified as

$$L(i_{\mathrm{L}}) = \frac{\Phi(I_{\mathrm{L}} + 0.5\Delta i_{\mathrm{L}}) - \Phi(I_{\mathrm{L}} - 0.5\Delta i_{\mathrm{L}})}{\Delta i_{\mathrm{L}}}. \tag{3.3}$$

Each computed value is referred to the measured average output current, defining an experimental differential inductance curve up to the saturation of the inductor under test. Figure 3.5 shows the measured differential inductance profile for the Coilcraft MSS1260T-273. In the same Figure are reported the profile determined with

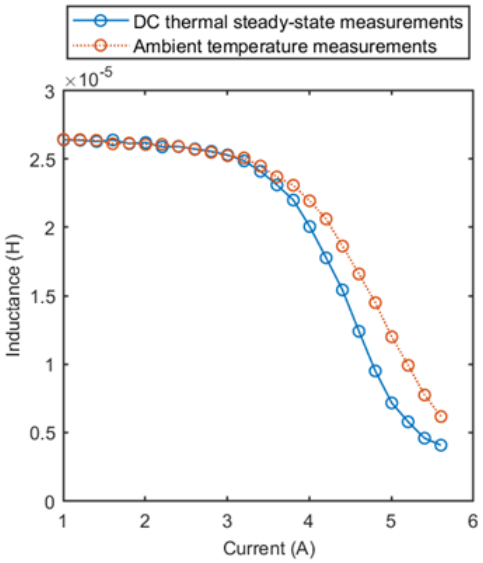

Fig. 3.5 Measured differential inductance profile of the Coilcraft MSS1260T-273. The orange profile is obtained from spot measurements with the inductor operating at ambient temperature. The blue profile represents the measurements performed considering the temperature rise caused by the DC-winding losses.

the proposed method and the one measured at ambient temperature, not reaching the steady-state temperature caused by the applied average output current. This comparison highlights how the effect of the over temperature determines a drop of the differential inductance value, more evident at high DC current values since the over temperature is increasing. In fact, the operating temperature strongly influences the differential permeability of a ferrite core. The saturation flux density of the material decreases as a function of the temperature, causing a rapid drop in the differential permeability profile. For these reasons, the characterisation performed at ambient temperature does not correctly describe the behaviour of a saturable inductor operating in a DC-DC converter, overestimating the differential inductance values

at high current values. The test conditions adopted for identifying the Coilcraft MSS1260T-273 are reported in Table 3.3.

Table 3.3 Test conditions for the Coilcraft MSS1260T-273.

Input voltage	24 V
duty cycle	0.5
Switching frequency	500 kHz
Output current	$1-5.6$ A

3.4 Parametrisation of the differential inductance curve

The differential inductance characterisation aims to adopt the non-linear inductor model in the circuit simulation of DC-DC converters to evaluate the saturable inductor operation. An analytical formulation of the differential inductance profile as a function of the applied current is more suitable for this aim, even considering commercial software or custom codes for the circuit simulations. The obtained experimental differential inductance value can be described by the formulation proposed in [24]

$$L(i_{\mathrm{L}}) = L_{\mathrm{L}} + \frac{L_{\mathrm{H}} - L_{\mathrm{L}}}{2}\{1 - \frac{2}{\pi}\arctan[\sigma(i_{\mathrm{L}}(t) - I_{\mathrm{L}}^{*})]\} \tag{3.4}$$

The parameters of the proposed formulation are:

- L_{L}, the lower horizontal asymptote of the differential inductance profile;
- L_{H}, the upper horizontal asymptote of the differential inductance profile;
- I_{L}^{*}, the abscissa of the inflection point of the curve, at which $L(I_{\mathrm{L}}^{*}) = \frac{L_{\mathrm{H}}+L_{\mathrm{L}}}{2}$;
- σ, a coefficient proportional to the slope of the differential inductance curve in I_{L}^{*}.

The curve fitting of the experimental characterisation can be easily performed through a deterministic pattern search optimisation algorithm [23]. The fitting process is fast,

and the obtained parametrised curve well describes the measurements. Figure 3.6 reports the parametrised differential inductance profile for the previously characterised inductor.

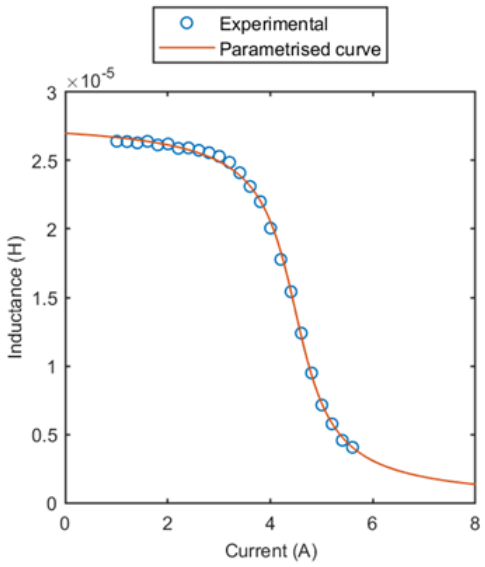

Fig. 3.6 Comparison of measured and the parametrised differential inductance profile for the Coilcraft MSS1260T-273.

The obtained $L(i_{\mathrm{L}})$ profiles can be adopted for the current waveform simulation of the saturable inductor operating in different input voltage, switching frequency and duty cycle conditions.

3.5 Simulation of the saturable inductor current waveforms

The evaluation of the saturable inductor operation in a DC-DC buck converter is performed by adopting the computation method proposed in [31], which uses the polarisation fixed point technique to solve the non-linear differential equations of the analysed system. A brief description of the proposed methodology is reported in Appendix C. The simulated and experimental current waveforms are compared for different input voltage, switching frequency and average output current values, which involve different DC and AC loss values of the inductor under test. As a remark, the identification procedure is performed with an input voltage $V_{\mathrm{in}} = 24$ V, a

switching frequency $f_{sw} = 500$ kHz, and a duty cycle $\delta = 0.5$. The setup adopted for the measurement is the same presented in 3.2, and the voltage and current waveforms are captured after obtaining the thermal steady-state condition of the part. For the first comparison, the switching frequency is varied, testing three values: 500 kHz, 750 kHz, 1 MHz. For all the mentioned switching frequency values, the average output current is regulated, spanning from the linear operation of the inductor under test, up to the deep saturation of the part. The results are reported in Figure 3.7a - 3.7c. In each Figure, the simulated and the measured current waveforms are represented in (a), while (b) and (c) report the relative error on the estimated RMS and peak value of the current, respectively.

The analysis of the presented results highlights the effectiveness of the DC thermal steady-state characteristic obtained over a wide range of switching frequency values. The relative error in estimating the current waveforms peak and RMS values is small, even considering the operation of the inductor towards the deep saturation of the magnetic core. Further verifications of the effectiveness of the proposed methodology are presented in Figures 3.8a and 3.8b, where the comparison at different input voltages are shown.

In particular, the measurements are performed at $V_{in} = 12$ V and $V_{in} = 32$ V. In this case, the switching frequency is fixed at $f_{sw} = 500$ kHz. Even in this case, the simulated and the measured current waveforms are represented in (a), while (b) and (c) report the relative error on the estimated RMS and peak value of the current. The effectiveness of the proposed identification method is confirmed even under different input voltage values. As a final remark, Figure 3.9 shows the measured and simulated waveforms for the Coilcraft MSS1260T-273 inductor while operating in linear condition and saturation. The three considered switching frequencies are presented. The effectiveness of the proposed method is confirmed even with the higher current ripple condition caused by the minimum switching frequency.

In appendix B the identification, parametrisation process, and current waveform computation are presented for the Coilcraft SER1390-333 inductor, which exhibits a different over-temperature behaviour as a function of the average current.

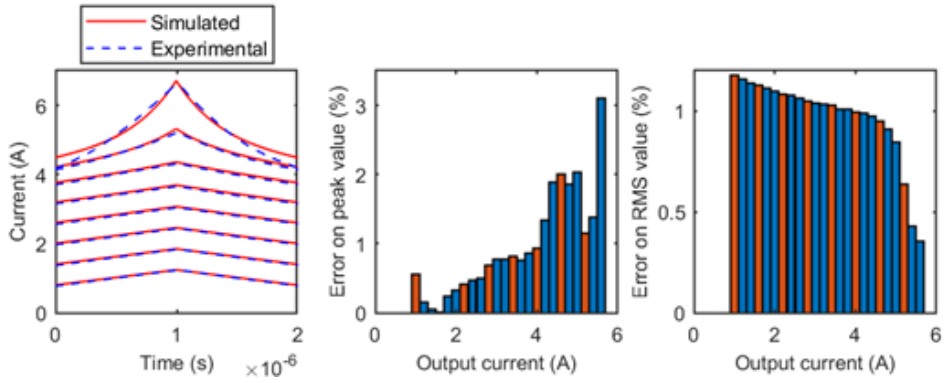

(a) $f_{sw} = 500\,\text{kHz}$

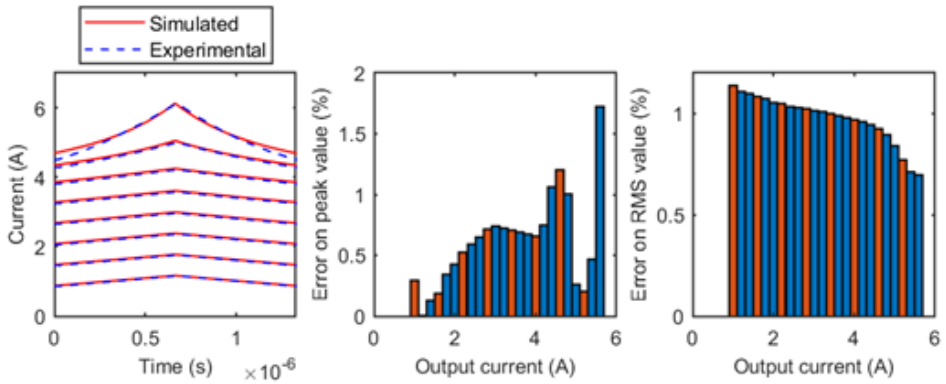

(b) $f_{sw} = 750\,\text{kHz}$

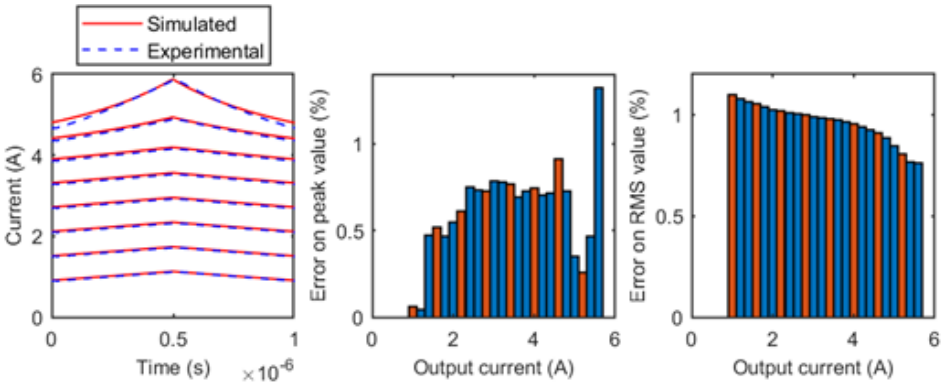

(c) $f_{sw} = 1\,\text{MHz}$

Fig. 3.7 Comparison of simulated and measured current waveforms under different switching frequencies for the Coilcraft MSS1260T-273. The comparison is presented for different average output current values up to the saturation of the inductor under test. The left plot represents the simulated and measured current waveforms. The central and right plots represent the relative error on the RMS and peak value estimation, respectively. Orange bars are relative to the average current values represented in the left plot.

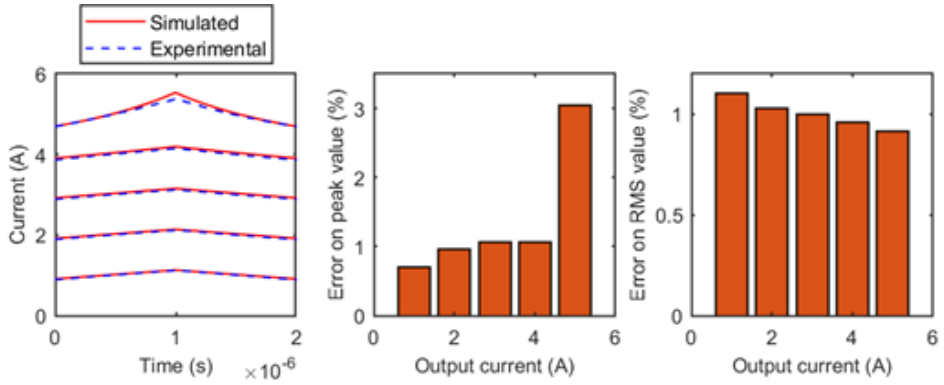

(a) $V_{\text{in}} = 12$ V

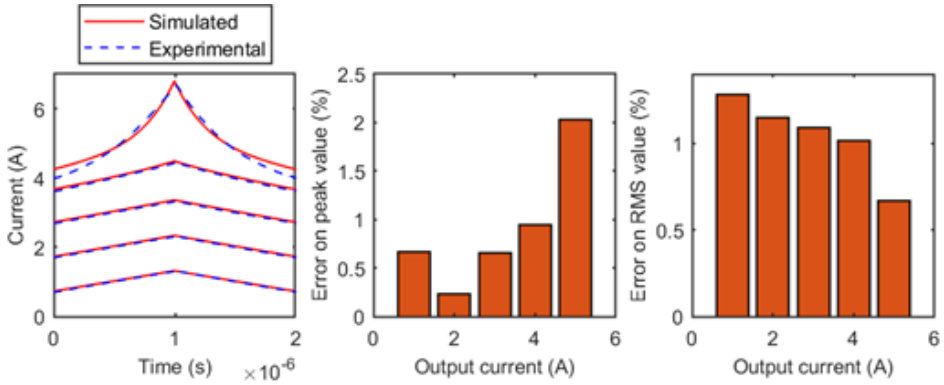

(b) $V_{\text{in}} = 32$ V

Fig. 3.8 Comparison of simulated and measured current waveforms under different input voltages for the Coilcraft MSS1260T-273. The comparison is presented for different average output current values up to the saturation of the inductor under test. The left plot represents the simulated and measured current waveforms. The central and right plots represent the relative error on the RMS and peak value estimation, respectively. Orange bars are relative to the average current values represented in the left plot.

3.6 Discussion and conclusions

The strength of the proposed approach is related to the limited set of experimental measurements required to identify the differential inductance profile of ferrite saturable inductors. The identification is performed by measuring inductor current and voltage waveforms under different average output currents with an experimental setup based on a commercial DC-DC converter. The basic assumption for the development of the proposed method is the correlation of the temperature variation of commercial saturable inductors to the average output current of the component, which is acceptable considering that saturable inductors operate at the upper limit of

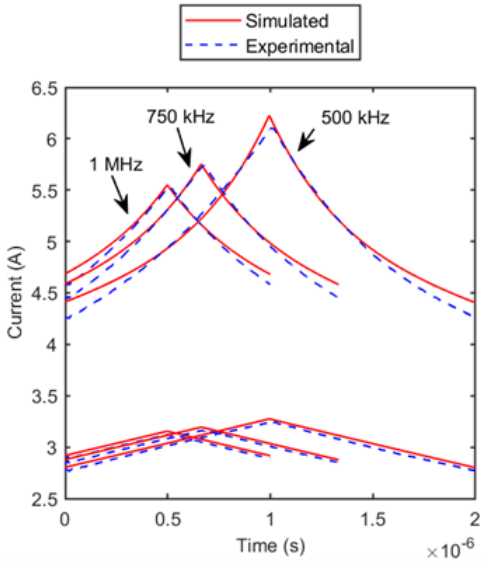

Fig. 3.9 Comparison of experimental and simulated current waveforms for different output current values and different switching frequencies for the Coilcraft MSS1260T-273.

their current range specification. More accurate thermal models to evaluate losses and inductance variation as a function of the over temperature are well described in the literature [32, 33]. However, these approaches are not easily applicable to commercial parts for which the specification of the core material, dimensions and winding properties are not available. In addition, the operating temperature of inductors is not an easily measurable quantity in the extremely close layouts of power converters.

The presented results demonstrate the crucial effect of DC winding losses on the temperature increase of inductors operating in saturation. Since the temperature of the ferromagnetic core strongly influences the core material, the differential inductance profile that considers the over-temperature caused by the average operating current is significantly different from the characteristic obtained at ambient temperature. The latter is the characteristic provided by manufacturers and determined from small signal spot measurements that do not consider the temperature variation. If this characteristic is adopted to evaluate the behaviour of saturable inductors operating in DC-DC converters, the results of the simulations should underestimate the effective current ripple at high output current. A characterisation approach for the differential inductance curve under the DC thermal steady-state conditions is presented to overcome this gap. The described identification methodology demon-

strates its effectiveness in representing the effective behaviour of ferrite commercial inductors operating in partial saturation over a wide range of output current, switching frequency and input voltage conditions. The obtained differential inductance profile allows for the simulation of the current waveforms of inductors operating in saturation even at average current values higher than the limit defined by the manufacturer. The simulated waveforms describe the experimental measurements well, and the error in estimating the peak and RMS value of the inductive current is always limited in the tested cases, never exceeding 3% under saturation conditions. The simulated and measured current waveforms are compared for different components under different winding and core loss values.

Chapter 4

Controlled variable inductors for WPT applications

Even if the knowledge of wireless energy transmission systems is ancient, and for decades wireless technology has been used in the field of telecommunication, the development of high-power wireless systems is recent, and it has been allowed by the development of high-frequency power electronic converters. Wireless Power Transfer (WPT) technology has been extensively developed in power applications in the last year. A WPT system allows transferring power from a source to a load avoiding the connection through bulky cables and connectors, which are parts exposed to deterioration during operations. In addition, a wireless solution guarantees higher comfort for the device's user. Innumerable factors have led this technology to become considerably popular in several fields, such as:

- Electric vehicles: WPT-based charging solutions for electric vehicles can be implemented through stationary solutions (with parked cars) or dynamic solutions (while the car is in motion). In particular, the latter case allows for improving the distance range of electric vehicles, reducing the size and the weight of the battery pack. This solution is particularly suitable for vehicles with predetermined driving paths, such as buses and trucks [34, 35].
- Health care: The use of wireless battery chargers for implantable electronic devices eliminates the wire connection between the power source and the devices, improving the safety of the patient. In addition, the adoption of

wireless chargers reduces the energy storage size of implantable devices, improving the patient's comfort.

- Consumer electronics: The massive diffusion of electronic devices (smartphones, tablets, wearable devices, laptops) has also pushed the development of WPT solutions for their charging [36, 37].

The list of WPT applications is not limited to the one presented. According to the physical principle behind power transfer, inductive and capacitive systems can be identified. For the sake of clarity, other methods for WPT systems are also diffused, such as radio frequency waves, optical links, and ultrasound. However, up to now, this methods are only used for signal transmission or very low-power transmission. In an Inductive Wireless Power Transfer (IWPT) system, the power is transferred through the time-varying magnetic field between coupled coils, a transmitter and a receiver. On the other hand, a Capacitive Wireless Power Transfer (CWPT) system converts energy through the time-varying electric field between capacitor electrodes. The IWPT technology is mature and widely adopted in commercial applications, both in the automotive and the portable electronic fields, while the CWPT is a relatively new technology, still under development, also from a standardisation point of view. Both technologies require a resonant compensation network to maintain high transmission efficiency. Compensation networks for WPT systems are made by a proper configuration of additional capacitors and inductors. However, the resonance of the system is typically tuned at a given coupling condition of the transmitter and receiver devices. A variation in the coupling caused by misalignment or variation in the distance of the parts determines a deviation from the resonance condition. An impedance matching of the compensation network allows the system to restore resonance conditions. To this end, a controlled variable inductor can be adopted to actively regulate the impedance of the compensation network, allowing the implementation of the magnetic control both for capacitive and inductive Wireless Power Transfer systems.

4.1 The magnetic control in IWPT systems

In an inductive system, the transmitter and the receiver coils are separated by a non-negligible air gap, whose length depends on the application. The air gap

determines high leakage flux, causing a low coupling coefficient of the coils. In order to improve the efficiency of the system, additional reactive components are adopted to implement resonant compensation networks. The most intuitive and widely adopted compensation topology for the IWPT system is the Series-Series (SS) compensation, implemented with a series capacitor on each coil side. However, several other topologies have been proposed in the literature to offer more degrees of freedom in the design and regulation of the system. In particular, the LCC-S topology ensures a lower voltage/current stress across the passive components compared to the SS compensation [38, 39]. The value of the input inductor in an LCC-S compensated WPT system influences the power transferred to the load. Thus, a controlled variable inductor (CVI) can be adopted to implement the output power regulation. This control technique is defined in the literature as the magnetic control (MC) technique, which is widely adopted in other resonant converter topologies, such as in the LLC or DAB resonant converters [40, 41]. The same concepts of magnetic control can be adopted to obtain an efficient regulation of the power transferred in the IWPT system. There are different ways to implement the magnetic control strategy. One is based on the reconfiguration of different discrete inductors through power switches. However, this solution is expensive and bulky since several components are required. In [42], a variable inductance is obtained, varying the air gap by inclined or stagged aperture structure mode. However, its manufacturing is complex, resulting in higher costs. An interesting approach consists of implementing a controlled variable inductor by controlling the magnetic permeability of the material using an additional magnetic polarisation flux in addition to the main inductor magnetic flux, shifting the magnetic induction [43]. A controlled variable inductor is obtained by preparing a ferromagnetic core with at least two windings. The first, defined as the main winding, is connected to the resonant tank of the WPT system, and the second, the auxiliary winding, allows to control the permeability of the core by regulating a magnetising current. In this way, the differential inductance of the main winding can be continuously regulated between an unsaturated and a saturated value. The strength of this approach is represented by the possibility of obtaining a wide differential inductance variation range through a single inductor, whose value can be regulated, reducing the size and weight of passive components if compared with the discrete inductor strategy. On the other hand, using a controlled variable inductor for the output power regulation in an IWPT system introduces some difficulties. The controlled variable inductor requires a DC current source to regulate the magnetising

current in the auxiliary winding effectively. Thus, an extra power converter is needed to implement the current control. A synchronous buck converter, operating at low voltage, is a suitable solution to supply the magnetising winding. A further critical aspect in using the CVI in the WPT system is related to the non-linear behaviour of the inductor when operating in the saturated condition. Proper inductor modelling is required to evaluate the WPT system performances in the design phase.

In order to evaluate the effectiveness of the magnetic control applied to an IWPT system, the equivalent circuit represented in Figure 4.1a is considered.

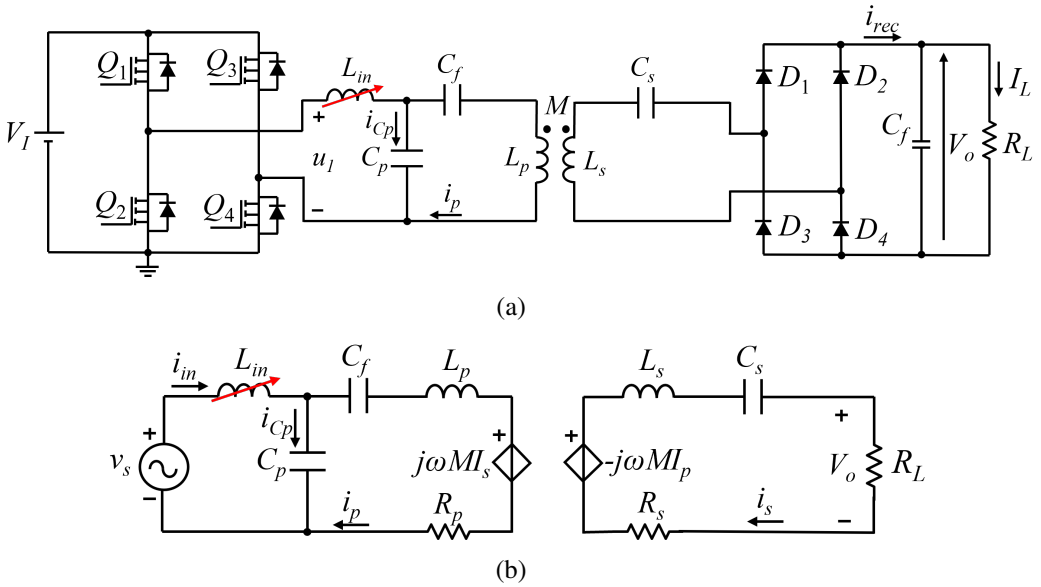

Fig. 4.1 (a) Circuit diagram of an LCC-S compensated WPT system. (b) Equivalent circuit of the first harmonic approximation of the system. R_p and R_s are the parasitic resistances of the primary and secondary coils.

A full bridge converter supplies the transmitter side of the system. The LCC compensation is considered on the primary side, while a series capacitor is adopted on the receiver side. A diode bridge rectifier converts the AC waveforms of the secondary side into the DC voltage required to supply an equivalent resistive load. The first harmonic approximation equivalent circuit, depicted in Fig. 4.1b, is used to determine the dependency of the output power and the efficiency of the system on the input inductance value. Appendix C reports the circuit description of an LCC-S compensated IWPT system, highlighting the dependence of the output power on the input inductance value. Considering a system with the specifications reported in

Table 4.1, the dependence of the output power on the input inductance value has the behaviour represented in Fig. 4.2.

Table 4.1 IWPT system parameters

Parameter	Value	Description
f_s	85 kHz	Operating frequency
V_I	24 V	DC input voltage
P_o	100 W	Output power
k	0.36	Coupling coefficient
L_p	86.7 μH	Primary coil inductance
R_p	0.82 Ω	Primary coil parasitic resistance
L_s	93.4 μH	Secondary coil inductance
R_s	0.71 Ω	Secondary coil parasitic resistance
R_L	50 Ω	Load resistance
C_f	46.2 nF	Filter capacitor
C_p	323.3 nF	Primary capacitor
C_s	37.5 nF	Secondary capacitor

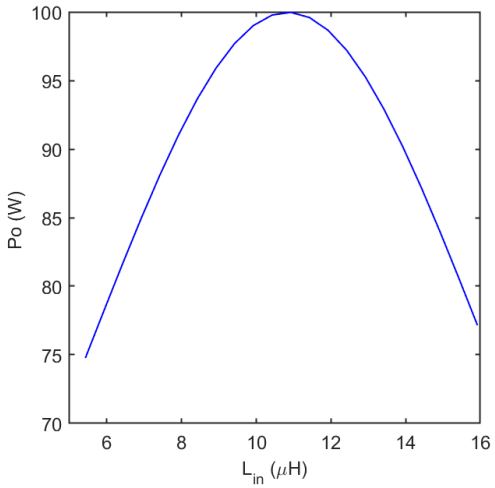

Fig. 4.2 Output power behaviour of an LCC-S compensated IWPT system, as a function of the input inductance value.

The figure highlights that the output power dependence on the input inductance has a symmetrical behaviour. The selected inductance variation range useful to

regulate the output power between 80 W and 100 W goes from an unsaturated value of 15 μH to a saturated value of 11 μH. A 27% variation determines the CVI operation in the partial saturation region. Thus, a non-linear model for the differential inductance profile of the CVI has to be considered. The procedure to obtain a suitable controlled variable inductor is described in 4.2

4.2 The design of a controlled variable inductor

A controlled variable inductor can be obtained by controlling the differential permeability of a ferromagnetic core, defined as the relative permeability corresponding to the slope at a given point on a magnetisation curve of magnetic flux density [44]:

$$\mu_{\mathrm{d}} = \frac{1}{\mu_0} \frac{\mathrm{d}B}{\mathrm{d}H}. \tag{4.1}$$

Figure 4.3 represents the DC magnetisation curve and the related differential permeability profile of the N87 ferrite. As highlighted in the figure, three operating regions can be identified:

- A linear region, where the differential permeability exhibits a near-constant profile.
- A roll-off region, where the differential permeability rapidly decreases.
- A saturated region, where the minimum value of the differential permeability is obtained.

In order to actively regulate the differential permeability of the core, an auxiliary winding is required to control the magnetic field value in the ferromagnetic material. The auxiliary winding is supplied by a DC current source able to regulate its value. An equivalent non-linear inductance model is used to determine the differential inductance profile of the controlled variable inductor [45]. In particular, considering a closed core shape with an N turns winding, the differential inductance is defined as

$$L_{\mathrm{d}} = \frac{\mathrm{d}\Phi}{\mathrm{d}i}. \tag{4.2}$$

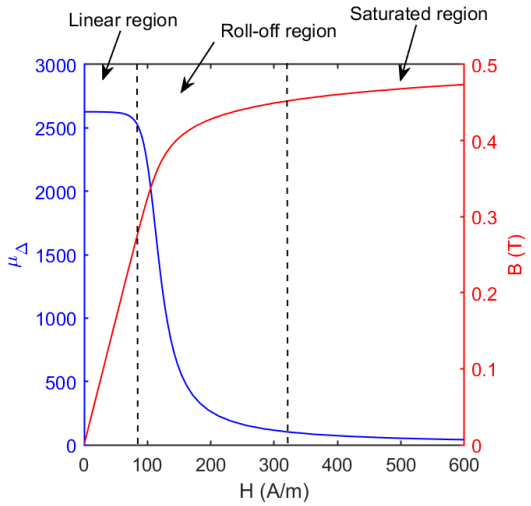

Fig. 4.3 Magnetisation curve and differential permeability profile of the N87 ferrite. The three operating regions of the magnetic material are highlighted.

If the cross-section S is assumed to be constant over the entire ferromagnetic path, the magnetic flux Φ is defined as

$$\Phi = N\,S\,B. \tag{4.3}$$

Ampere's Law determines the relation between the applied current i and the related magnetic field H:

$$i = \frac{H\,l_{\mathrm{fe}}}{N}. \tag{4.4}$$

Thus the differential inductance can be directly related to the differential permeability of the core:

$$L_{\mathrm{d}} = N^2 \frac{S}{l_{\mathrm{fe}}} \frac{\mathrm{d}B}{\mathrm{d}H} = N^2 \frac{S}{l_{\mathrm{fe}}}\,\mu_0\,\mu_\Delta = \frac{N^2}{\mathscr{R}_{\mathrm{eq,d}}}. \tag{4.5}$$

The core shape considered for the design of the controlled variable inductor is the double E geometry. With this configuration, the path of the static magnetic field can be controlled only on the outer legs of the core. Two DC windings with $0.5\,N_{\mathrm{DC}}$ turns connected in anti-series and placed on the outer legs allow to control the differential permeability of the ferromagnetic material of the outer path of the core from the linear region up to the saturated region of the magnetisation curve. The main winding, also defined as the AC winding, is placed on the central leg of the core. The material of the central leg operates in the linear region of the magnetisation

curve, since no static magnetic field interests this path, and an air gap ensures low AC magnetic field values even with considerable voltage and current swings of the AC winding [43]. Figure 4.4 represents a 2D FEM simulation of the proposed double E core configuration when only the auxiliary windings are supplied. The magnetic flux path and the magnetic flux density colour map highlight how the core's central leg is practically not involved in the magnetic flux applied by the DC windings. Moreover, the anti-series connection of the outer leg windings almost cancels the sum of the AC electromotive force on each DC winding.

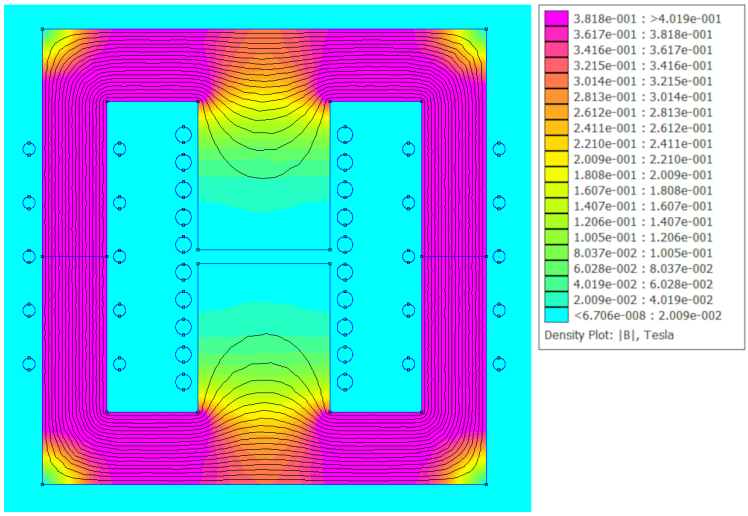

Fig. 4.4 Magnetic flux density distribution obtained by FEM simulation of the proposed double E core. Only the auxiliary windings on the outer legs are supplied. The DC magnetic flux path involves only the outer legs of the core.

4.2.1 Analytical design procedure

In order to obtain the differential inductance profile suitable for the application specification, the equivalent reluctance model represented in Figure 4.5 is used to compare different core sizes, air gap lengths, number of turns of the DC and the AC windings.

The equivalent differential reluctance, reported in (4.5) and referred to the AC winding, can be computed as

$$\mathscr{R}_{\mathrm{eq,d}} = \mathscr{R}_{\mathrm{tot,c}} + 0.5\,\mathscr{R}_{\mathrm{tot,l}}, \tag{4.6}$$

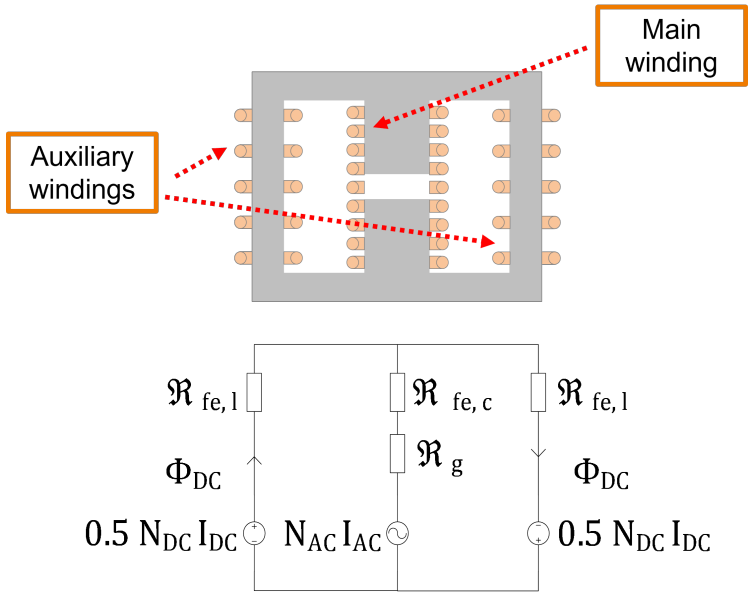

Fig. 4.5 Description of the core and winding configuration for the controlled variable inductor design. (a) Adopted double E core gapped configuration. (b) Equivalent reluctance circuit.

where

$$\mathscr{R}_{\text{tot,c}} = \frac{l_{\text{fe,c}}}{\mu_0\,\mu_{\text{fe,in}}\,S_{\text{fe,c}}} + \frac{l_{\text{g}}}{\mu_0\,S_{\text{g}}} \tag{4.7}$$

and

$$\mathscr{R}_{\text{tot,l}} = \frac{l_{\text{fe,l}}}{\mu_0\,\mu_{\text{fe,d}}\,S_{\text{fe,l}}}. \tag{4.8}$$

The value of $\mu_{\text{fe,in}}$, adopted in the computation of the ferromagnetic path reluctance of the central leg in (4.7), is the initial permeability value of the ferromagnetic material. The differential permeability $\mu_{\text{fe,d}}$, adopted in the computation of the ferromagnetic path reluctance of the outer leg in (4.8), is a function of the DC magnetomotive force applied by the auxiliary winding, that determines the magnetic field strength. The differential inductance profile of the controlled variable inductor can be finely tuned to regulate the WPT system's power transfer by controlling this parameter.

The gap cross-section S_{g} of (4.7) is corrected in order to consider the fringing field's effects on the equivalent gap reluctance, as [46]

$$S_{\text{g}} = (a + l_{\text{g}}) \cdot (b + l_{\text{g}}), \tag{4.9}$$

where a and b are the two dimensions of the central column cross-section.
For a given core geometrical configuration, the dependence of the differential permeability on the magnetomotive force is determined by solving the equivalent non-linear reluctance model through the polarisation fixed point technique, as reported in Appendix A. Table 4.2 describes the specifications considered for the controlled variable inductor used in the magnetic control of the IWPT system analysed in 4.1.

Table 4.2 Design parameter of the controlled variable inductor prototype for IWPT.

Core material	N87 ferrite
Core geometry	E 32/16/9
Gap length	1 mm
AC winding N turns	10
DC winding N turns	10 $(5+5)$

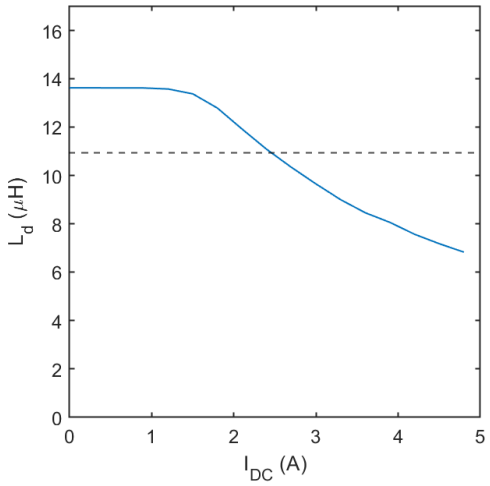

Fig. 4.6 Differential inductance profile as a function of the magnetising current, computed with the analytical reluctance model for the prototype defined in Table 4.2

The selected ferromagnetic material for the core of the CVI is a ferrite since, in this kind of application, a rapid saturation of the core is required, with low values of the magnetising current. The saturation profile of the obtained structure is tuned by means of the air gap that regulates the equivalent reluctance path of the central leg in order to obtain a controllable differential inductance profile. In addition, the

high-frequency voltage and current waveforms applied by the IWPT system require a core material with excellent specific loss properties to maintain the high efficiency of the transmission system. Based on these considerations, the N87 ferrite is an appropriate choice. Figure 4.6 represents the computed differential inductance profile of the configuration reported in Table 4.2.

4.2.2 Simulation verification of the analytical design

A magnetostatic 2D FEM simulation of the considered geometry is performed through the software FEMM to validate the differential inductance profile provided by the analytical computations. The simulation is performed in different steps, increasing the DC current value in the auxiliary windings, while the AC winding is supplied with a small signal current to determine the differential inductance value. Figure 4.7 compares the analytical computation and the FEM simulation output.

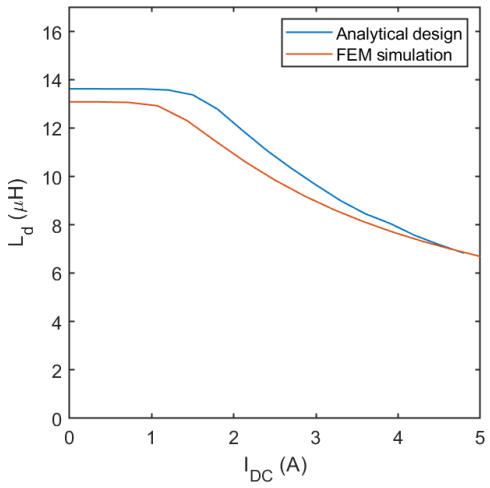

Fig. 4.7 Comparison of the differential inductance profile obtained with the analytical reluctance model and the one obtained from FEM simulations.

The reluctance model adopted for the analytical computation does not consider the leakage flux paths and cannot effectively consider the reluctance of the air gap, even introducing the gap section correction reported in (4.9). On the other hand, the finite element simulation well describes and considers these phenomena. However, the deviation between the two differential inductance curves can be considered negligible if compared to the effect of the tolerances on the geometrical dimensions

of the core and particularly on the permeability value of the magnetic material, which will be encountered in the manufacturing of the CVI prototype. In conclusion, the considered design specification is assumed to be suitable to effectively implement the magnetic control strategy for the proposed IWPT system, and thus they are considered to realise the prototype of the controlled variable inductor. Since he proposed CVI operates with AC waveforms at 85 kHz, skin and proximity effects appear in the conductors of the AC winding. The high-frequency resistance increase of the main winding can cause a non-negligible increase in the ohmic losses, which would affect the overall efficiency of the energy transmission system. In addition, the non-negligible concentrated air gap in the central leg of the E core could further accentuate the presented problems due to the high magnetic field present in the gap region [14]. Figure 4.8 represents the current density distribution of the AC winding. The effect of the magnetic field spread near the air gap is apparent, and the simulation highlights the current density increase in this region. Considering a winding cross-section of 1 mm^2, the resistance at 85 kHz is 24 times the DC resistance. Ferrite cores with distributed air gaps could be a partial solution to

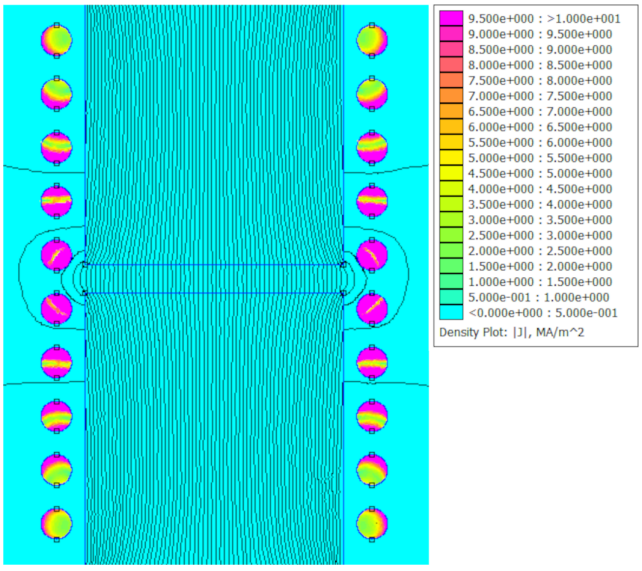

Fig. 4.8 Current density distribution in the wire of the main winding, at 85 kHz. The conductors in the air gap region are interested by higher current density values.

mitigate the fringing flux effect reducing the length of each gap and thus reducing the losses caused by the proximity effect and eddy currents. However, this solution is not adopted in manufacturing the CVI inductor prototype. A practical solution to mitigate the high-frequency resistance increase in the main winding is adopting a litz

wire. The litz wire is a multistrand wire composed of many thin strands, individually insulated and twisted together. The effect of this structure is the equalisation of the current distribution among the wire strands, reducing the AC resistance of the winding. The diameter of the strands should be selected according to the supply frequency to make the skin effect in the single strand negligible. At 85 kHz, the skin depth in a copper wire is about 0.22 mm. Thus, a wire diameter of 0.1 mm allows to mitigate the issue related to skin effect considerably. Considering an equivalent 1 mm^2 section made of 130 twisted strands with a diameter of 0.1 mm, the AC over DC resistance ratio reduces to 2.16 without involving an increase in the DC resistance. The high-frequency resistance of the auxiliary winding is not critical because only a reduced AC current component can circulate due to the induced electromotive force. In addition, a non-zero resistance on the auxiliary winding is also desirable to reduce the AC current that can circulate in the DC supply circuit due to the unbalance of the electromotive forces of the two half winding, which will be further described. For this reason, a solid conductor with a cross-section of 0.6 mm^2 is selected for the auxiliary windings.

The described specification of the controlled variable inductor is adopted to implement a circuit simulation of the IWPT system that takes into account the non-linear behaviour of the magnetic component. The commercial software PLECS® is adopted to this aim. The controlled variable inductor is described with saturable core blocks, representing the ferromagnetic path reluctance, and air gap blocks. However, the standard saturable core blocks of PLECS® only describe the magnetisation curve of the material using a *coth* based or a *atan* based fitting function, which in our experience do not well describe the differential permeability profile of the N87 ferrite. Therefore, a custom saturable core block is implemented through a look-up table approach. The equivalent non-linear reluctance model of the considered double E core can be simulated, considering the interaction with the electrical circuit of the IWPT system. Figure 4.9 represents the equivalent circuit of the LCC-S compensated IWPT system and the model of the controlled variable inductor adopted in PLECS® for the circuit simulation.

The circuit simulation allows to:

- Validate the principle of the magnetic control of the LCC-S compensated IWPT system.

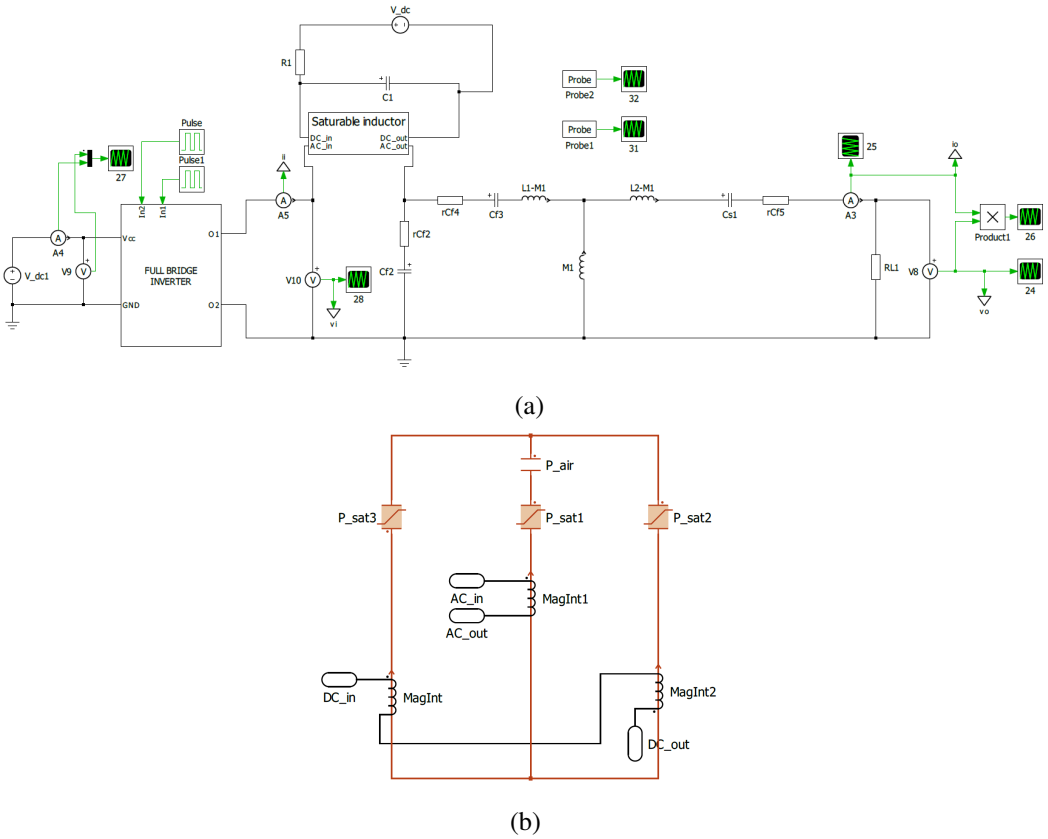

Fig. 4.9 (a) Equivalent circuit adopted for the PLECS® simulation of the LCC-S compensated IWPT system. (b) Detail of the controlled variable inductor model in PLECS®.

- Verify the operating conditions of the magnetic material for the different paths under the typical operating waveforms of the system.

Figure 4.10 shows the voltage and current waveforms applied on the CVI during the typical operation of the IWPT system.

The effectiveness of the magnetic control is taken into account by varying the magnetising current from zero up to the value required to regulate the input inductance at 11 μH. The IWPT operates with the nominal input DC voltage and the nominal load condition. Figure 4.11a represents the average power transferred to the load in the unsaturated and then in the saturated operation of the controlled variable inductor. In addition, Figure 4.11b shows the magnetising current required to saturate the component. The simulation confirms that the load power transfer can be effectively regulated by controlling the auxiliary winding current of the CVI. The transient response of the system appears to be fast and well damped. The circuit

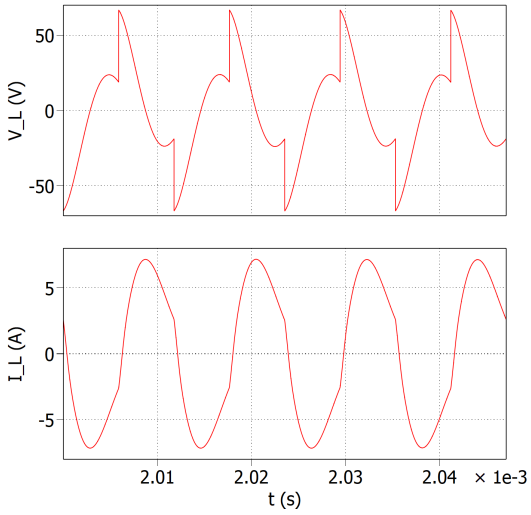

Fig. 4.10 Simulated voltage and current waveforms on the CVI in the LCC-S compensated IWPT system.

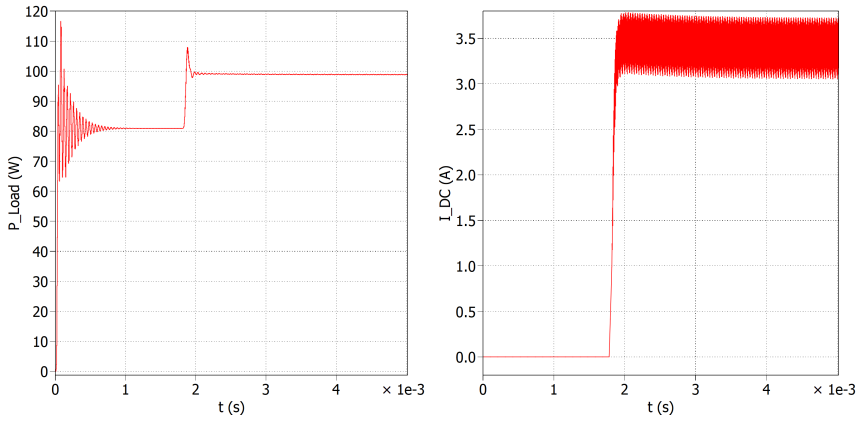

(a) (b)

Fig. 4.11 (a) Average power transferred to the load in the unsaturated and saturated operation of the controlled variable inductor. (b) Related magnetising current profile in the auxiliary windings.

simulation helps to verify the magnetic flux swing in the three core legs and the operating point of the ferromagnetic material of the different paths in the saturated operation. The results are represented in Figure 4.12, where the operating region of the central and the outer legs is reported on the magnetisation curve of the N87 ferrite, and in Figure 4.13, where the simulated magnetic flux waveforms are represented for the three paths, during the unsaturated and the in the saturated operation. As

predicted in the magnetic design phase, the central leg operates in the linear region of the magnetisation curve, while the outer legs operate in the roll-off region.

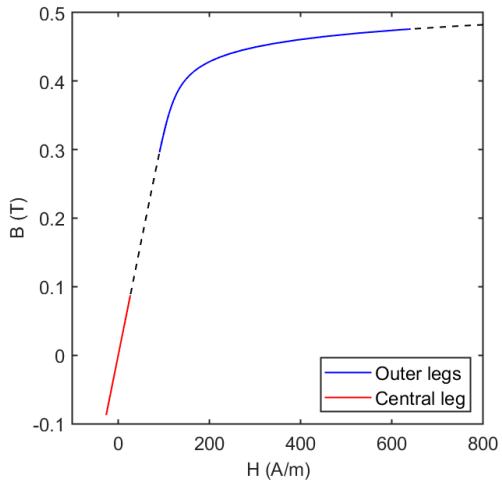

Fig. 4.12 Operation regions of the magnetic material in the saturated case. The central leg operates in the linear region of the magnetisation curve, while the outer legs operate in the roll-off region.

The circuit simulation also highlights a drawback of the double E core configuration. When the material of the outer legs operates in the roll-off region of the magnetisation curve, the introduced non-linearity causes the electromotive force on each magnetisation winding to be not symmetrical, and a residual AC voltage is applied to the DC supply circuit. Figure 4.14 represents an example of the induced voltages on the DC windings when the ferromagnetic material of the outer leg operates in the linear region or the roll-off region of the magnetisation characteristic.

In the saturated case, the sum of the electromotive force on the magnetisation windings, connected in anti-series, results in a non-zero AC voltage which determines a high-frequency current component in the power supply circuit. This high-frequency current, also visible in Figure 4.11b, could interact with the regulation system of the magnetising current control. If the number of turns of the AC and DC windings is adequately selected, the presented issue can be reduced. In addition, as previously mentioned, the adoption of a solid wire for the DC winding, when stimulated with a high-frequency supply, allows for damping the AC current due to the increased resistance value caused by the skin and proximity effect. All the

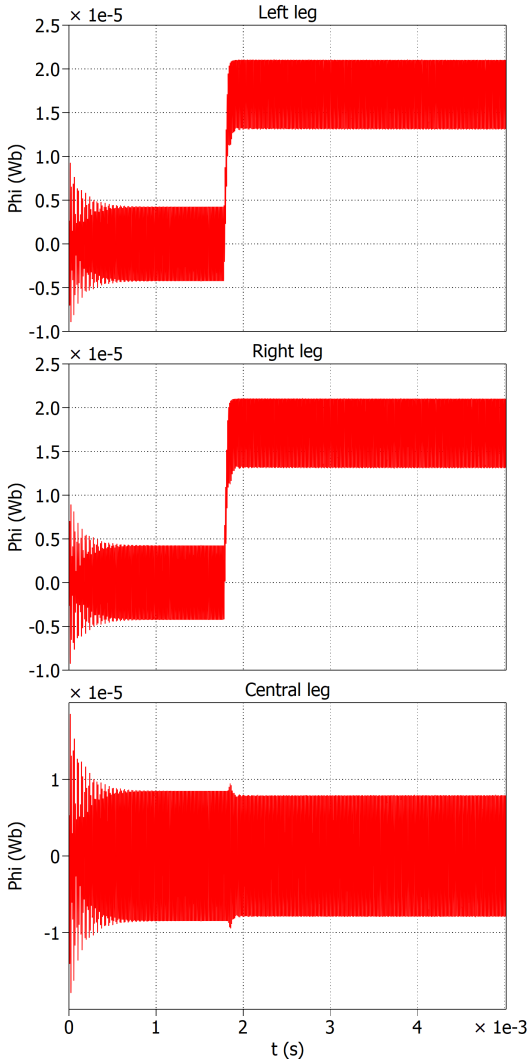

Fig. 4.13 Magnetic flux waveforms in the three core legs during the unsaturated and saturated operation.

performed simulations confirm the effectiveness of the proposed design of the CVI inductor, and a prototype is realised to perform an experimental validation of the magnetic control. Figure 4.15 shows a photo of the CVI prototype.

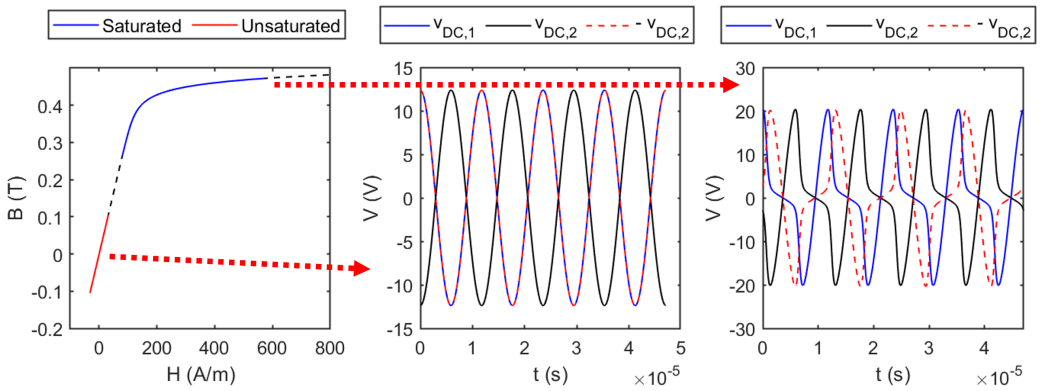

Fig. 4.14 Induced voltages on the DC windings when the ferromagnetic material of the outer leg operates in the linear region or the roll-off region of the magnetisation characteristic. In the first case, the sum of the induced voltages on the auxiliary windings is zero, while a non-zero voltage holds in the second.

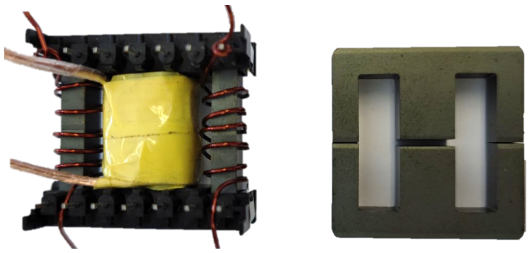

Fig. 4.15 Photo of the CVI prototype. The adopted N87 ferrite core with a gapped central column is on the right.

4.2.3 Experimental validation of the analytical design

The specifications of the CVI are measured to validate the proposed design. In particular, the differential inductance profile is measured as a function of the magnetising current. The adopted setup is composed of the Hioki IM3536 LCR meter to measure the impedance of the main winding and a controllable DC source to regulate the current in the magnetising winding. In principle, the main and auxiliary windings are not mutually coupled due to the anti-series connection of the two DC windings. This scheme should compensate the overall induced electromotive force. Thus no AC current should flow in the auxiliary winding. In this case, the magnetisation circuit does not represent a load for the main winding, not perturbing the impedance measurement. However, as previously stated, going toward the saturation of the core, the sum of the electromotive forces on the anti-series of the two DC windings is

no more null. A 2 mH ferrite choke with high saturation current is placed in series with the magnetisation circuit to ensure that the auxiliary winding connections do not influence the measurement. Since the measurement is performed at 85 kHz, the impedance of the choke, in addition to the high-frequency resistance of the magnetisation circuit, is considered sufficient to avoid the differential inductance measurement perturbation. Figure 4.16 represents the measured differential inductance profile compared with the analytical reluctance model and the FEM simulation output.

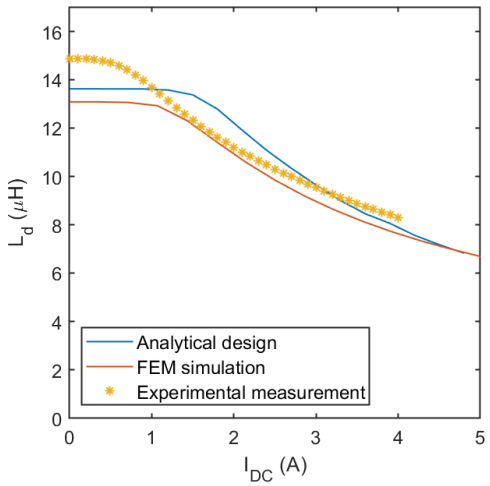

Fig. 4.16 Measured differential inductance profile of the CVI prototype, compared with the analytical reluctance model and the FEM simulation output.

As the figure shows, the measured differential inductance profile exhibits some differences with the predicted behaviour. The motivations can be found, besides the approximation of the analytical reluctance model and the 2D FEM simulation, in the high tolerances on the permeability values of N87 ferrite that the core manufacturer declares (typically $\pm 25\%$ to the nominal values), in addition to the more limited tolerances on the geometrical dimensions of the core and on the air gap length (typically $\pm 5\%$ to the nominal values). Since these parameters strongly influence the differential inductance value, the differences between the design results and the measurements can be motivated. Moreover, the positioning of the winding on the magnetic core determines the leakage and fringing flux effects, which are phenomena difficult to model during the design phase. However, the differential inductance profile obtained by the experimental measurements is suitable for the

specifications of the considered LCC-S compensated IWPT system since the initial value and the inductance variation required are satisfied. The LCR meter also allows the measurement of the resistance of the main winding as a function of the supply frequency. This measurement is useful to verify the resistive losses at the resonance frequency of the IWPT system [47] and to validate the proper selection of the litz wire specification. The frequency behaviour measurement of the winding resistance is a critical task since the real part of the measured impedance also considers the power losses of the core. Considering that the separation of the winding and the core loss terms requires more accurate measurements and models of the magnetic loss behaviour, the AC resistance of the winding is measured without the ferromagnetic core. In order to perform the measurement, the winding is placed on the coil former but is not positioned on the magnetic core. In this case, the obtained resistance value will be underestimated. In fact, the magnetic field distribution in the winding region is strongly influenced by the effect of the core, and in particular near the air gap region. Removing the core will alter the magnetic field density with respect to the real operating condition. However, this kind of measurement, even if not significant on the specific resistance value, is still helpful to determine the effectiveness of the selected litz wire strand diameter. The so-measured behaviour of the main winding resistance as a function of the supply frequency is presented in Figure 4.17.

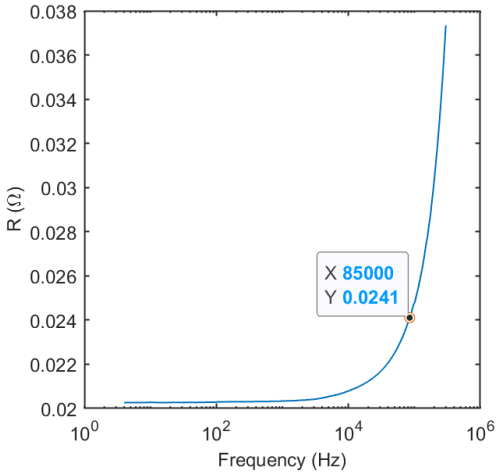

Fig. 4.17 Measured AC winding resistance as a function of the frequency.

At the resonance frequency of the WPT system, a 19% increase with respect to the DC resistance is reported in the tested configuration. This increase is not considered a critical issue for the efficiency of the IWPT system under test.

4.3 Test of the CVI in the experimental IWPT system

The effectiveness of the proposed magnetic control strategy in the WPT field is verified by testing the CVI prototype in an experimental LCC-S compensated IWPT system. The experimental setup, that has the specification reported in Table 4.1, is depicted in Figure 4.18.

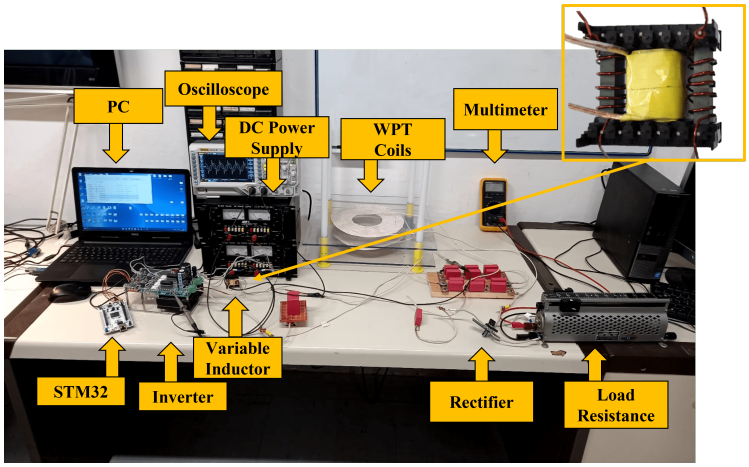

Fig. 4.18 Photo of the experimental setup.

The proposed results are obtained not operating the setup at full power configuration. The magnetising current is controlled in an open-loop configuration, and the DC windings are supplied with a controllable DC source. The positioning of the transmitter and receiver coil is fixed, and the operating frequency is constant at $f_{sw} = 85$ kHz. Further tests are in progress. In order to validate the principle of magnetic control in the IWPT system, the power transferred to the load is measured in the unsaturated and saturated operation. The traces of Figures 4.19a and 4.19b represent the measured voltage waveforms on the controlled variable inductor in the saturated and the unsaturated condition and the voltage applied on the parallel capacitor C_{in} of the LCC-S compensation network.

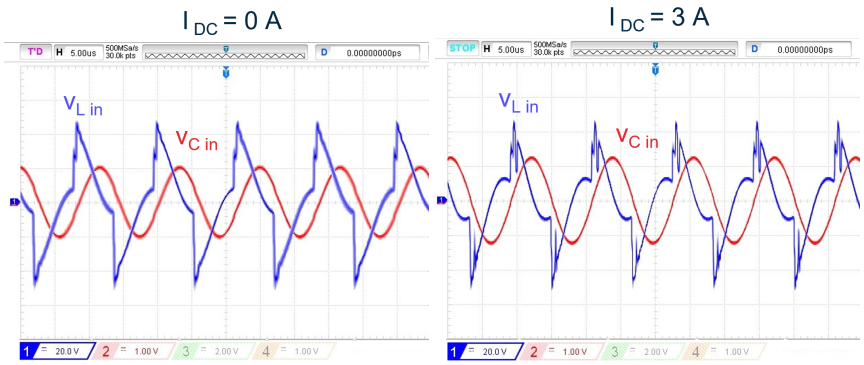

(a) (b)

Fig. 4.19 Measured voltage waveforms on the controlled variable inductor and on the input capacitor. (a) Unsaturated operation. (b) Saturated operation.

Table 4.3 reports the measured output power and the magnetising current applied to obtain the required inductance value.

Table 4.3 Measurements on the experimental IWPT system

	$\mathbf{P}_{\text{load}}$ (W)	$\mathbf{I}_{\text{DC}}$ (A)
Unsaturated	34.94	0
Saturated	53.66	3

The preliminary experimental results confirm the ability to regulate the output power of the system by controlling the input inductance value using a controlled variable inductor. Further considerations should be made on the efficiency of the IWPT system, mainly when the inductor operates in the saturated condition.

4.4 Analysis of the DC current regulator

The regulation of the magnetising current is a critical aspect of the proposed magnetic control strategy since the DC winding circuit represents an inductive load with low series resistance (at zero frequency). The supply system of the magnetising windings should also have a high efficiency and a low cost. The regulation of the magnetising current can be obtained through a linear or switching approach.

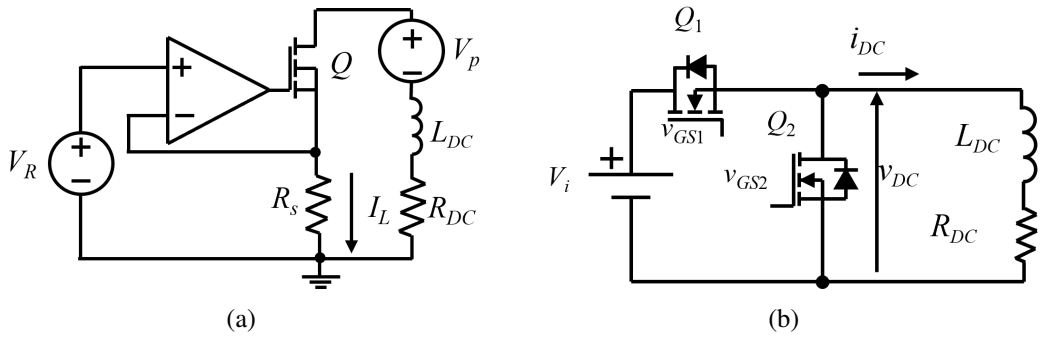

Fig. 4.20 Schemes for the magnetising current regulation of the CVI. (a) Linear regulation (b) Switching regulation.

A linear control circuit presents a very stable and precise current regulation. Moreover, the cost for its implementation is generally lower than a switching solution, requiring a single transistor. However, the linear solution is characterised by higher losses than a switching approach. In the literature, extensive analyses of the circuit represented in Figure 4.20a are proposed [48, 49]. The main drawback of the presented solution is the power dissipated on the transistor operating in the linear region, particularly when a high magnetising current is required. In order to maintain high transmission efficiency, a DC-DC switching converter can be adopted, significantly reducing the power losses of the magnetisation circuit. A further advantage of the switching solution, represented in Figure 4.20b, is the reduced size that increases the power density of the auxiliary circuit. The load of the auxiliary supply circuit is represented by the DC winding resistance of the controlled variable inductor, which has a value of $R_{\mathrm{DC}} = 74.3\ \mathrm{m\Omega}$. The magnetising current range required to regulate the output power of the IWPT system is $I_{\mathrm{DC}} = (0-3)$ A, thus the steady state output voltage ($V_{\mathrm{DC}} = R_{\mathrm{DC}} \cdot I_{\mathrm{o}}$)) will be in the range $V_{\mathrm{DC}} = (0-223)$ mV. This considerably low value requires switching devices with extremely low voltage drops. An input voltage of $V_{\mathrm{i}} = 3.3$ V is chosen to avoid the operation with an extremely low duty cycle. The switching circuit can be implemented using low current and low breakdown voltage MOSFETs operating in synchronous buck converter topology [50]. However, for reducing the current ripple, an increase in the switching frequency of the DC-DC converter would be beneficial, as illustrated in Figure 4.21.

In addition, an higher switching frequency for the supply of the magnetising current also allows a more precise current regulation. For this reason, a switching frequency $f_{\mathrm{s}} = 500\,\mathrm{kHz}$ is chosen. At this frequency value, GaN FETs are suitable for

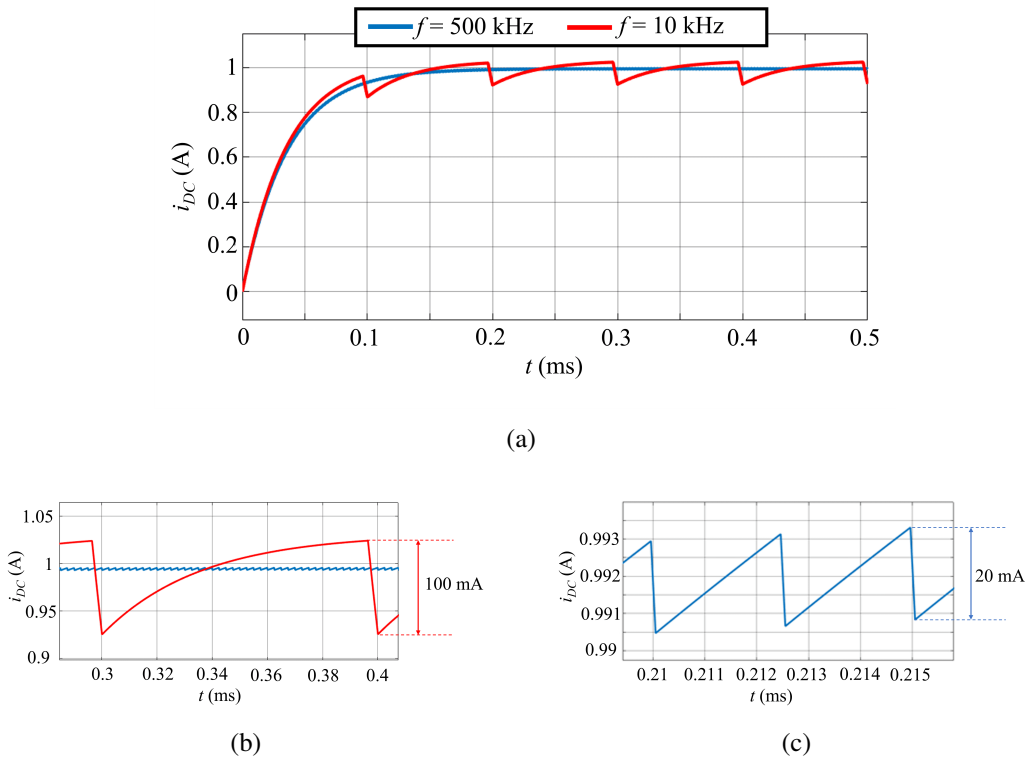

Fig. 4.21 Simulated transient behaviour of the magnetising current, with two different switching frequencies of the DC-DC converter. (a) Comparison of the two switching frequencies. (b) 10 kHz. (c) 500 kHz.

this application [51]. A simulation of the DC current regulator circuit is performed, adopting the model of the EPC2111 consisting of an enhancement-mode GaN power transistor. Figure 4.22 represents the power losses of the current regulator at $f_s = 500$ kHz for different operating currents.

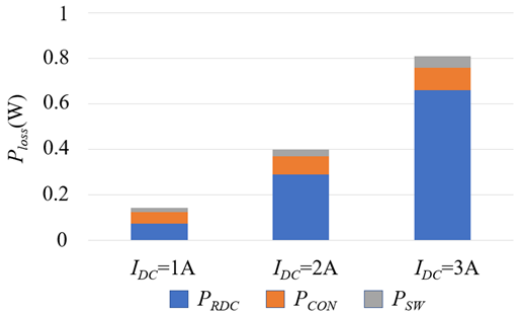

Fig. 4.22 Power losses of the auxiliary circuit for different operating current values.

The main loss term is dissipated on the parasitic resistance of the winding (P_{RDC}). Thanks to the use of GaN power switches, both the conduction (P_{CON}) and switching losses (P_{SW}) are limited. The obtained value of losses is considered satisfactory for the efficiency of the considered IWPT system. The proposed study must be further investigated to determine an effective closed-loop control strategy for output power regulation. The saturation of the CVI precludes the analysis of the control system using the traditional linear system approach. A potentially suitable solution could be the adoption of measure-based look-up tables to correlate the inductance value of the CVI to the required magnetising current and, in particular, to the required output power of the system.

4.5 Discussion on magnetic control for IWPT

The adoption of controlled variable inductors is diffuse in the field of resonant converters to implement the magnetic control strategy of the output power. The presented analysis proposed the use of magnetic control in IWPT systems. In particular, the variation of the input inductance value allows the implementation of an output power regulation without the need to adjust the switching frequency of the full bridge adopted for the supply of the transmission side. The operation at a fixed switching frequency allows the switching components and the resonant passive components to be optimised for the design frequency. The impedance adaptation of the system is assigned to the controlled variable inductor, whose differential inductance value can be finely regulated operating on the magnetising current of an auxiliary winding. The effectiveness of the output power regulation through adjusting the input inductance value is validated with simulations and experimental measurements. In addition, the auxiliary circuit for the magnetising current regulation can be designed to guarantee low power losses using a high-frequency GaN-FET based synchronous buck converter, ensuring high overall transmission efficiency. An open task related to adopting a CVI for the output power regulation of IWPT is the analysis of the power losses of the component when operating in saturated conditions. The analysis is not trivial since the different section of the magnetic core operates at different magnetic flux density values and under different magnetic field bias conditions. In addition, the closed-loop regulation strategy to control the

output power as a function of the applied magnetising current value must be further investigated.

4.6 The use of the CVI in CWPT systems

The Capacitive Wireless Power Transfer technology is assuming increasing importance in the scenario of charging systems low power applications, in the field of portable electronics, robots, drones, and biomedical plants [52]. The capacitive technology has some advantages if compared to the IWPT, such as:

- The reduced eddy current losses.
- The ability to transfer power through isolated metal objects.
- The reduced cost of capacitive plates if compared to litz wire coils.
- The lower power dissipation and heat production.

However, the CWPT technology still needs to be developed and more standardised compared to IWPT [53]. Nevertheless, in recent years, great interest in this technology has been emerging in the literature and applications. The magnetic control strategy also finds a place in regulating the Zero Voltage Switching (ZVS) and Zero Current Switching (ZCS) operations in a capacitive wireless power transfer system [54]. In a CWPT system, the misalignment between the metallic plates highly influences the coupling between the transmitter and receiver. The coupling variation strongly affects the power transferred to the load and the efficiency of the transmission. As for the inductive systems, a resonant compensation network is required to ensure high efficiency. Since the coupling between the transmitter and receiver side is provided through a capacitive system, the most intuitive compensation scheme involves at least an inductor. The regulation of the inductance value allows the tuning of the system to resonate at a fixed frequency under different values of the capacitive coupling between the metallic plates, in order to guarantee a high transmission efficiency. The proposed analysis investigates a CWPT system supplied by a Class-E inverter with an LC compensation network [55]. The Class-E inverter structure is implemented with a single semiconductor device (a MOSFET or a GaNFET) that can operate in the Zero Voltage Switching (ZVS) and Zero

Current Switching (ZCS) conditions, if properly designed, leading to low switching losses. However, the ZVS/ZCS operation is highly influenced by the capacitive coupling between the metallic plates. A method to cover a wide range of capacitive coupling variations maintaining the ZVS/ZCS operation consists of the regulation of the passive components of the resonant network. In particular, considering the LC compensation scheme, the proposed approach is implemented with a matrix of capacitors for the resonant and the shunt capacitor and a controlled variable inductor for the resonant inductor.

The electrical scheme of the Class-E inverter adopted for the CWPT system is represented in Figure 4.23.

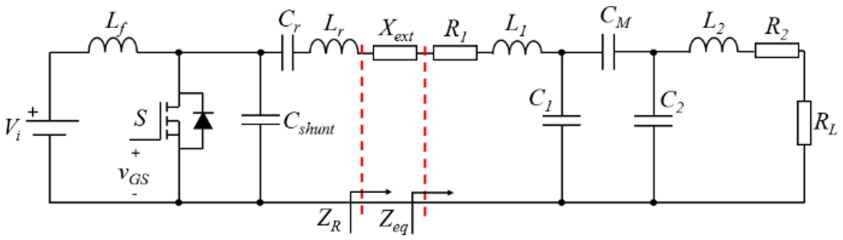

Fig. 4.23 Equivalent circuit of a CWPT system supplied with a Class-E inverter topology, with the LC compensation scheme on the transmitter and the receiver side.

The coupling between the capacitive plates is represented by the capacitance C_{M}, assuming that the cross-coupling capacitances between the plates can be neglected. An LC compensation scheme is adopted for the transmitter and the receiver side. The capacitors C_1 and C_2 are designed to resonate with the inductances L_1 and L_2. The ZVS/ZCS operation is reached when the equivalent impedance Z_{R} exhibits a purely resistive behaviour. However, the resonant operation is negatively influenced by the misalignment between the capacitive plates, reducing the transferable output power and the system's efficiency. In this topology, the resonant inductance L_{r}, resonant capacitance C_{r}, and shunt capacitance C_{shunt} values required to maintain the Class-E inverter operating at ZVS/ZCS depend on the equivalent load resistance and coupling capacitance value. The specifications of the analysed setup are reported in Table 4.4.

Table 4.4 CWPT system parameters

Parameter	Value	Description
f_s	200 kHz	Operating frequency
P_o	50 W	Output power
R_L	5 Ω	Load resistance
Q_L	10	Quality factor
$C_{m^{opt}}$	200 pF	Coupling capacitance (nominal value)
$ESR_{Lf1,Lf2,L1,L2,}$	100 mΩ	Inductances parasitic resistances
L_1, L_2	100 μH	Primary and secondary inductances
C_1, C_2	6.3 nF	Primary and secondary capacitances
C_{ext}	327.3 nF	External capacitance
C_r	48 nF	Resonant capacitance (nominal value)
C_{shunt}	77 nF	Shunt capacitance (nominal value)
L_r	14.9 μH	Resonant inductance (nominal value)

The proposed control strategy regulates the resonant and shunt capacitances through a matrix of capacitors. The resonant inductance variation is obtained through a CVI. Figure 4.24 represents the values of the resonant inductor, the resonant capacitor and the shunt capacitor required to operate in the ZVS/ZCS condition as a function of the capacitive coupling.

As represented in Figure 4.24b and 4.24c, the range of variation of the coupling capacitance is divided into three parts. Depending on the operating condition, a particular capacitor is selected. The methodology adopted to design the CVI is the same proposed in 4.2, and the specification required for the component is an inductance variation in the range 20 μH – 10 μH, at a switching frequency of 200 kHz. Also in this case, litz wire is adopted to reduce the series resistance of the main winding. Table 4.5 reports the configuration of the controlled variable inductor used for the output power regulation of the CWPT system.

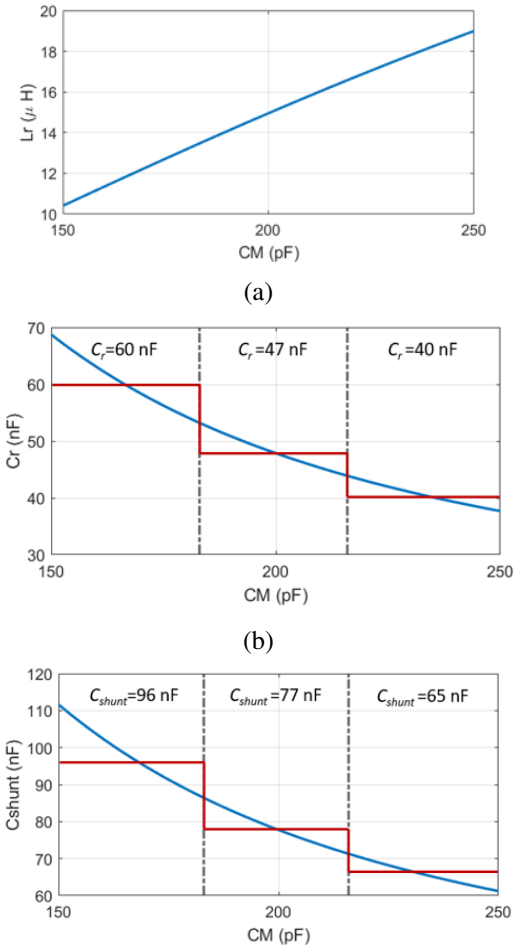

Fig. 4.24 Effect of the coupling coefficient variations on the required values of resonant network components. (a) Resonant inductance L_{r}. (a) Resonant capacitor C_{r}. (a) Shunt capacitor C_{shunt}

Table 4.5 Design parameter of the controlled variable inductor prototype for CWPT.

Core material	N87 ferrite
Core geometry	E 25/13/7
Gap length	0.5 mm
AC winding N turns	12
DC winding N turns	10 $(5+5)$

Figure 4.25 represents the computed differential inductance profile of the configuration reported in Table 4.5.

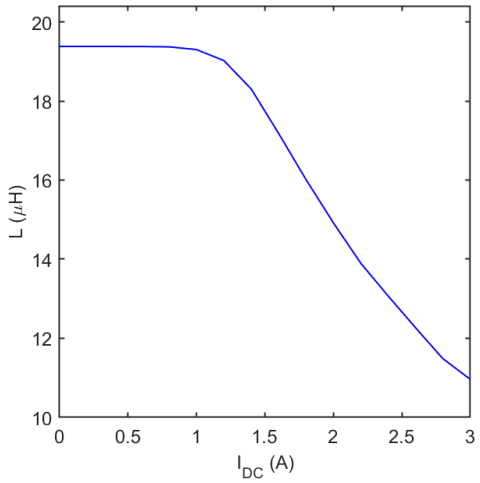

Fig. 4.25 Differential inductance profile as a function of the magnetising current, computed with the analytical reluctance model for the prototype defined in Table 4.5

The software PLECS® is used to simulate the CWPT system with the variable resonant component. The controlled variable inductor is described with saturable core blocks, representing the ferromagnetic path reluctance, and air gap blocks. The equivalent non-linear reluctance model of the considered double E core can be simulated, considering the interaction with the electrical circuit of the CWPT system. Figure 4.26 represents the behaviour of the output power comparing the adoption of the variable reactive component approach to the fixed component approach. The proposed control strategy effectively keeps the output power at the target value over a wide range of coupling capacitance values. On the other hand, when the reactive components of the compensation network are fixed, the output power is close to the target value only when the system operates close to the nominal coupling component value.

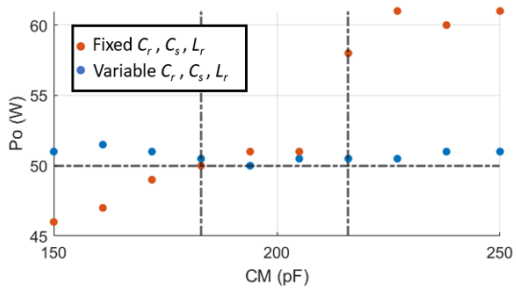

Fig. 4.26 Simulated power losses of the CWPT system comparing the variable reactive component control strategy to the fixed component approach, when the capacitive coupling of the plates varies.

Figure 4.27 represents the same comparison applied to the conversion efficiency of the CWPT system. Also in this case, the proposed control technique maintains higher values over the whole capacitive coupling range since the system constantly operates in ZVS/ZCS conditions.

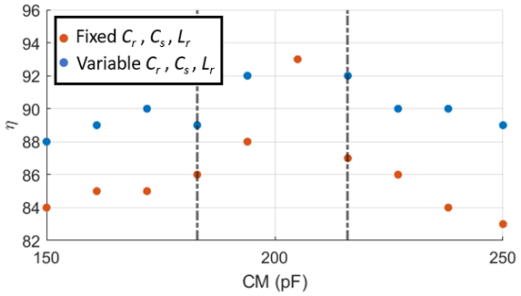

Fig. 4.27 Simulated efficiency of the CWPT system comparing the variable reactive component control strategy to the fixed component approach, when the capacitive coupling of the plates varies.

4.7 Discussion on magnetic control for CWPT

Adopting a controlled variable inductor in the compensation network of a CWPT system is a suitable solution to operate in ZVS/ZCS conditions over a wide range of capacitive coupling, whose variation is caused by the misalignment between the metallic plates. The maintained operation near the ZVS/ZCS conditions guarantees high transmission efficiency. The same considerations on the magnetisation circuit supply system proposed in 4.4 can be assessed even in the case of the CVI for CWPT. However, the resonant tank inductor variation is insufficient to guarantee

the ZVS/ZCS condition, and even the series and the shunt capacitor values have to be adapted as a function of the coupling between the metallic plates. Further analyses are required to limit the adaptation to the shunt capacitor in parallel with the resonant tank. In addition, an experimental system is under development to test the effectiveness of the promising results obtained with circuit simulations.

Chapter 5

Conclusions

This thesis deals with several challenges related to the design and use of magnetic components in power electronics converters. In particular, the analysis of inductors for DC-DC converters is addressed. The main design requirements of these devices are driven by efficiency and power density. With this in mind, the sizing of the inductor, which is responsible for a significant share of the converter's losses and volume, must be adequately addressed. To this end, the analysis of the design of a buck converter output inductor is proposed in Chapter 2, highlighting the effect of core material properties on the design result and proposing loss minimisation strategies based on the specific volume requirements of the design. The investigation also highlights the multi-objective nature of the problem addressed, which aims to minimise two conflicting goals, volume and losses. In order to adequately address the problem, a multi-objective approach is presented to reduce the computational cost of the problem. Indeed, it is emphasised that the feasibility evaluation of a design configuration, represented by the evaluation of the differential inductance profile, represents the most computationally demanding task of the optimisation procedure. Moreover, this evaluation is applied to a large number of design configurations, the majority of which do not comply with the constraints. This high computational cost is avoidable. To this end, the feasibility evaluation through an AIS-based classifier is proposed. The preliminary results show excellent possibilities for reducing the computational cost of the optimisation problem addressed. However, some open tasks still need to be solved. One of these is undoubtedly the adequate characterisation of the losses of the materials adopted for manufacturing inductor cores. In particular, given the lack of information from manufacturers, to improve the analysis of losses of

inductors operating in DC-DC converters, an in-depth experimental characterisation campaign is needed to determine the effect of the DC bias magnetic field on losses. In addition, given the tendency to operate at increasingly higher switching frequencies, a better understanding and modelling of high-frequency effects in the windings of magnetic components is also essential. Regarding the classification supported multi-objective optimisation, despite the promising results from the analysis of an AIS-based classifier, different classification methodologies can be tested to improve the approach to the feasibility evaluation problem.

Maximising the power density of inductors for DC-DC converters can also be accomplished by operating these magnetic components in partial saturation. In fact, for the same operating inductance required, the use of inductors in partial saturation allows the adoption of smaller volume cores. However, in order to correctly assess in the design phase the operation of these devices, which will operate in the non-linear region of the magnetisation characteristic, knowledge of the differential inductance profile is required, which is usually not provided by the manufacturers. For this purpose, a setup of experimental characterisation of the differential inductance profile of commercial inductors for DC-DC converters is proposed in Chapter 3. The characterisation is also performed by taking into account the effect of losses on the over-temperature of the component and, thus, on the permeability of the magnetic material. Therefore, the methodology applied for measuring and processing the experimental differential inductance characteristic is described, and a useful parameterisation for the circuit simulation of non-linear inductors is proposed. The results are very satisfactory when applied to ferrite inductors in the hundreds of Watt range (12-24 V, $\approx$ 10 A). Further developments of this study should go in the direction of evaluating its effectiveness on inductors for higher power applications (12-24 V, $\approx$ 50 A). In this case, powder cores inductors are preferred to ferrite inductors, which have different loss properties, magnetisation characteristics, and construction features.

The inductance variation value of saturable inductors can also be used to implement control techniques for resonant converters. The use of controlled variable inductors for magnetic control is widely discussed in the literature in the case of LLC-type or DAB-type converters. In Chapter 4, the magnetic control strategy for resonant Wireless Power Transfer structures is proposed. In particular, the analysis and dimensioning of a controlled variable inductor to implement the regulation of the transferred power in an inductive WPT system is presented, demonstrating its

effectiveness through the realisation of an experimental setup. This study requires further investigation in the analysis of the closed-loop control of the transferred power WPT system, realised through the regulation of the magnetising current of the saturable inductor. In addition, the preliminary study of using a variable inductor to regulate capacitive WPT systems is also proposed. In this case, the activity, verified through analytical investigations and simulations, should be appropriately validated with experimental verifications.

Appendix A

The polarisation fixed point technique

This method allows describing the magnetic flux density in the core material through a linearly dependent term on the magnetic field, multiplied by a constant permeability value μ_{fp}, and a residual term B_{res} to which the non-linearity is allocated:

$$B = \mu_0 \mu_{\text{fp}} H_{\text{fe}} + B_{\text{res}}. \tag{A.1}$$

Considering that

$$H_{\text{fe}} = \frac{B}{\mu_0 \mu_{\text{fp}}} - \frac{B_{\text{res}}}{\mu_0 \mu_{\text{fp}}} \tag{A.2}$$

and

$$H_{\text{gap}} = \frac{B}{\mu_0}, \tag{A.3}$$

(2.6) can be expressed as

$$NI = \left(\frac{B}{\mu_0 \mu_{\text{fp}}} - \frac{B_{\text{res}}}{\mu_0 \mu_{\text{fp}}} \right) l_{\text{fe}} + \frac{B}{\mu_0} l_{\text{gap}}, \tag{A.4}$$

From which the magnetic flux density value for the application of the iterative method can be calculated:

$$B^{\mathrm{k}+1} = \frac{NI + \frac{B^{\mathrm{k}}_{\mathrm{res}}}{\mu_0 \mu_{\mathrm{fp}}} l_{\mathrm{fe}}}{\frac{l_{\mathrm{fe}}}{\mu_0 \mu_{\mathrm{fp}}} + \frac{l_{\mathrm{gap}}}{\mu_0}}. \tag{A.5}$$

Once the magnetic flux density value at step $\mathrm{k}+1$ has been determined, the corresponding magnetic field value can be calculated from (A.2):

$$H^{\mathrm{k}+1} = \frac{B^{\mathrm{k}+1}}{\mu_0 \mu_{\mathrm{fp}}} - \frac{B^{\mathrm{k}}_{\mathrm{res}}}{\mu_0 \mu_{\mathrm{fp}}}. \tag{A.6}$$

The magnetic field value is used to update the residual term by exploiting the magnetization curve defined by the manufacturer:

$$B^{\mathrm{k}+1}_{\mathrm{res}} = B_{\mathrm{data}}(H^{\mathrm{k}+1}) - \mu_0 \mu_{\mathrm{fp}} H^{\mathrm{k}+1}. \tag{A.7}$$

The iterative technique is terminated when the residual flux density value for two successive steps does not show any significant variation. The convergence of the method is ensured for any initial value of the residual term B_{res}, that at the first iteration is set to zero, and its value will be iteratively adjusted following (A.7). The constant term μ_{fp}, however, should be accurately selected. In particular, the condition

$$\mu_{\mathrm{fp}} = \frac{\mu_{\mathrm{fe,max}} + \mu_{\mathrm{fe,min}}}{2} \tag{A.8}$$

ensures the optimal convergence of the method.

Appendix B

Identification results on Coilcraft SER1390-333

The inductor Coilcraft SER1390-333 is tested to evaluate further the results of the identification method proposed in 3. The test conditions are reported in Table B.1

Table B.1 Test conditions for the Coilcraft SER1390-333.

Input voltage	24 V
duty cycle	0.5
Switching frequency	500 kHz
Output current	$1-6.2$ A

The experimental identification process and the parametrisation of the differential inductance curve are effective, as represented in Figure B.1. Figure B.2a-B.2c report the comparison of the measured current waveforms and the simulated ones for the three considered switching frequencies: 500 kHz, 750 kHz, 1 MHz. The input voltage is $V_{\text{in}} = 24$ V and the duty cycle is $\delta = 0.5$. Figures B.3a and B.3b report the same comparison at fixed switching frequency $f_{\text{sw}} = 500$ kHz and duty cycle $\delta = 0.5$, varying the input voltage value (12 V and 32 V, respectively). The presented results confirm the effectiveness of the proposed identification method, showing even better performances in the simulation of the current waveforms under different operating conditions due to the lower over-temperature reached by the SER1390-333 during the operation in a DC-DC buck converter.

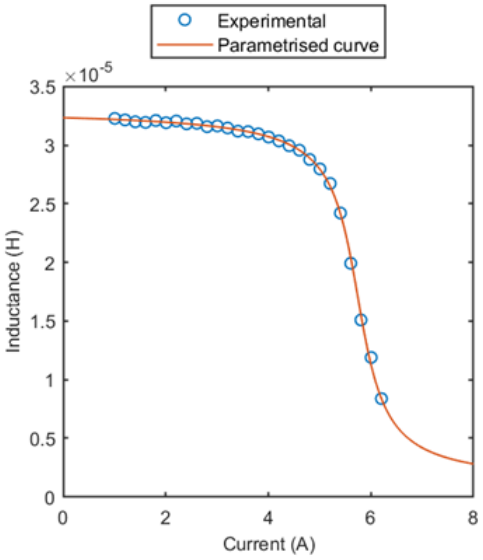

Fig. B.1 Comparison of measured and the parametrised differential inductance profile for the Coilcraft SER1390-333.

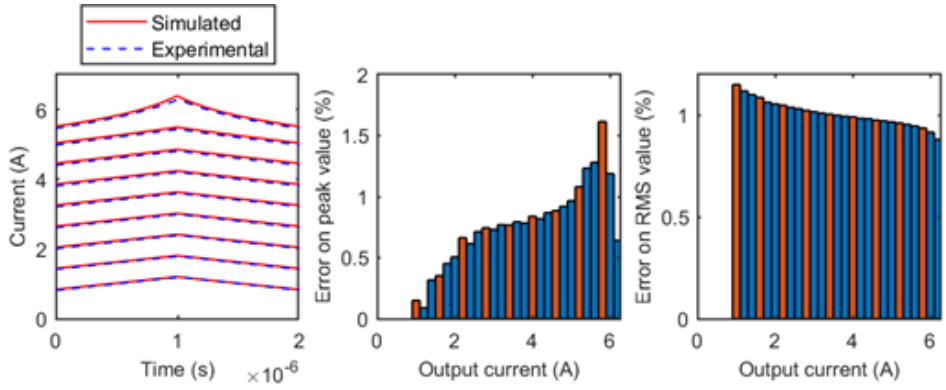

(a) $f_{sw} = 500$ kHz

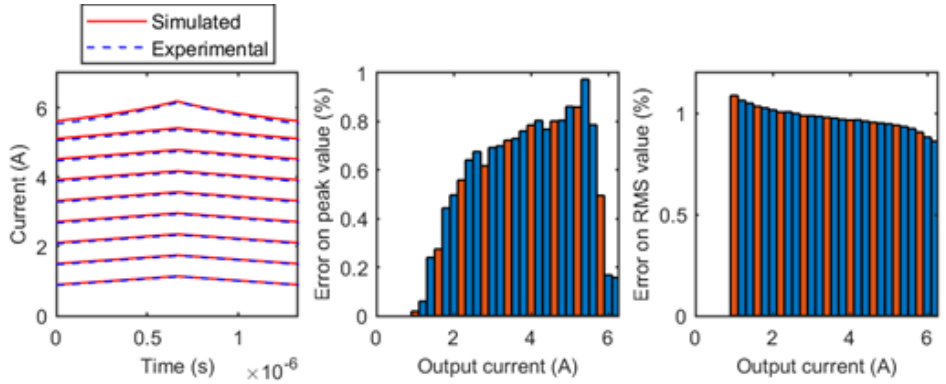

(b) $f_{sw} = 750$ kHz

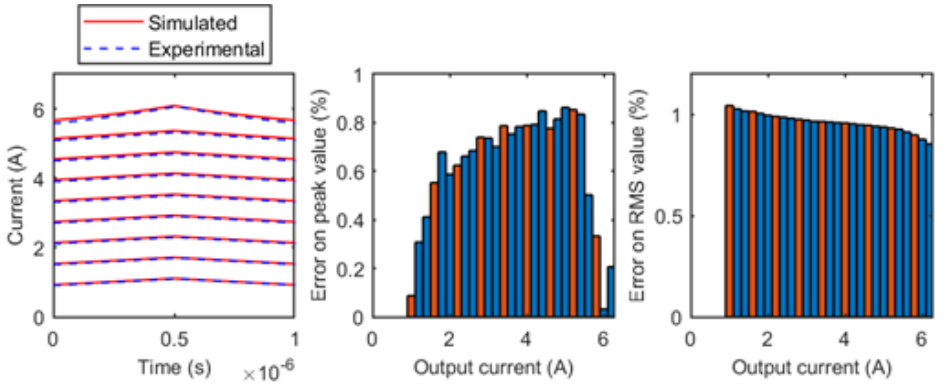

(c) $f_{sw} = 1$ MHz

Fig. B.2 Comparison of simulated and measured current waveforms under different switching frequencies for the Coilcraft SER1390-333. The comparison is presented for different average output current values up to the saturation of the inductor under test. The left plot represents the simulated and measured current waveforms. The central and right plots represent the relative error on the RMS and peak value estimation, respectively. Orange bars are relative to the average current values represented in the left plot.

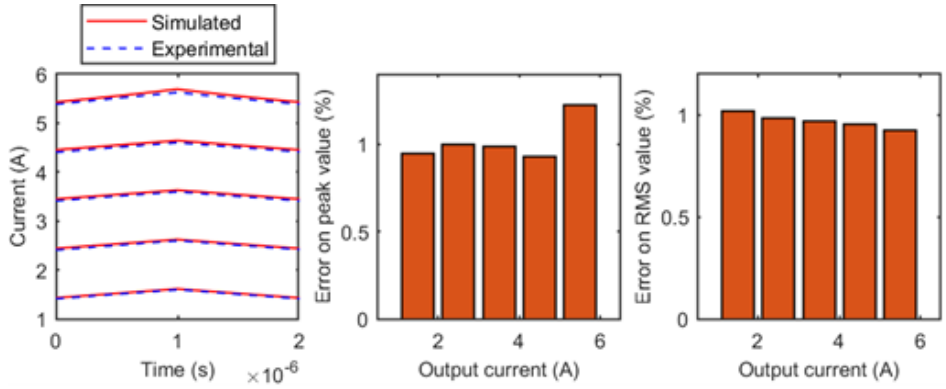

(a) $V_{\text{in}} = 12$ V

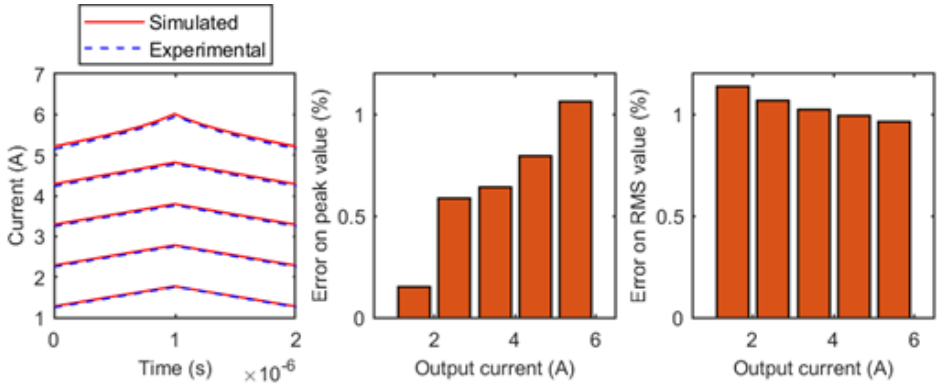

(b) $V_{\text{in}} = 32$ V

Fig. B.3 Comparison of simulated and measured current waveforms under different input voltages, for the Coilcraft SER1390-333. The comparison is presented for different average output current values up to the saturation of the inductor under test. The left plot represents the simulated and measured current waveforms. The central and right plots represent the relative error on the RMS and peak value estimation, respectively. Orange bars are relative to the average current values represented in the left plot.

Appendix C

Analysis of the LCC-S compensated IWPT system

The relationships between capacitors and inductors, which allow to obtain the maximum power transfer and minimise the reactive power circulating in the system, are

$$L_{\mathrm{s}} = \frac{1}{\omega_0^2 C_{\mathrm{s}}}, \tag{C.1}$$

$$L_{\mathrm{in}} = \frac{1}{\omega_0^2 C_{\mathrm{p}}}, \tag{C.2}$$

$$L_{\mathrm{in}} = L_{\mathrm{p}} - \frac{1}{\omega_0^2 C_{\mathrm{f}}}. \tag{C.3}$$

Analysing the circuit shown in Fig. 4.1b, the output power can be defined as

$$P_0 = \frac{\omega^2 M^2 V_{\mathrm{s}}^2 R_{\mathrm{L}}}{R^2 \omega^2 k_1^2 + k_2^2 k_5^2} \tag{C.4}$$

and the transmission efficiency is

$$\eta = \frac{\omega^2 M^2 R_{\mathrm{L}} C_{\mathrm{f}}}{R k_2 \left\{ C_{\mathrm{p}} k_4 + k_5 (C_{\mathrm{p}} + C_{\mathrm{f}} k_6) \right\}}, \tag{C.5}$$

where

$$k_1 = L_{\mathrm{in}} + L_{\mathrm{p}} - \frac{1}{\omega^2 C_{\mathrm{f}}} + \frac{C_{\mathrm{p}} L_{\mathrm{in}}}{C_{\mathrm{f}}} - \omega^2 C_{\mathrm{p}} L_{\mathrm{in}} L_{\mathrm{p}}, \tag{C.6}$$

$$k_2 = \omega^2 M^2 + R_\mathrm{p} R, \tag{C.7}$$

$$R = R_\mathrm{L} + R_\mathrm{S}, \tag{C.8}$$

$$k_3 = 1 - \omega^2 L_\mathrm{p} C_\mathrm{f}, \tag{C.9}$$

$$k_4 = \omega^2 C_\mathrm{f}(L_\mathrm{in} + L_\mathrm{p}) + \omega^2 L_\mathrm{in} C_\mathrm{p} k_3 - 1, \tag{C.10}$$

$$k_5 = 1 - \omega^2 L_\mathrm{in} C_\mathrm{p}, \tag{C.11}$$

$$k_6 = 1 - \omega^2 L_\mathrm{p} C_\mathrm{p}. \tag{C.12}$$

M is the transformer coupling factor and V_s is the RMS value of the voltage v_s.

References

[1] Goldman, Alex. *Magnetic Components for Power Electronics*. Springer Verlag, 2013. OCLC: 829754052.

[2] Muhammad H. Rashid, editor. *Power electronics handbook*. Energy engineering and power technology. Butterworth-Heinemann, an imprint of Elsevier, Amsterdam, fourth edition edition, 2018.

[3] William G. Hurley and Werner H. Wölfle. *Transformers and inductors for power electronics: theory, design and applications*. Wiley, Chichester, reprinted with corrections edition, 2014.

[4] Juergen Biela, Uwe Badstuebner, and Johann W. Kolar. Impact of Power Density Maximization on Efficiency of DC–DC Converter Systems. *IEEE Transactions on Power Electronics*, 24(1):288–300, January 2009.

[5] Scott D. Sudhoff. *Power magnetic devices: a multi-objective design approach*. IEEE press series on power and energy systems. Wiley, Hoboken, NJ, second edition edition, 2022.

[6] Luigi Solimene, Carlo Stefano Ragusa, and Salvatore Musumeci. The role of materials in the optimal design of magnetic components for DC–DC converters. *Journal of Magnetism and Magnetic Materials*, 564:170038, December 2022.

[7] M. Chiampi, D. Chiarabaglio, and M. Repetto. An accurate investigation on numerical methods for nonlinear magnetic field problems. *Journal of Magnetism and Magnetic Materials*, 133(1):591–595, May 1994.

[8] Luke Milner and Gabriel A. Rincón-Mora. Small saturating inductors for more compact switching power supplies. *IEEJ Transactions on Electrical and Electronic Engineering*, 7(1):69–73, 2012. _eprint: https://onlinelibrary.wiley.com/doi/pdf/10.1002/tee.21697.

[9] Jeremias Kaiser and Thomas Dürbaum. An Overview of Saturable Inductors: Applications to Power Supplies. *IEEE Transactions on Power Electronics*, 36(9):10766–10775, September 2021.

[10] Bin Chen, Xu Liang, and Nina Wan. Design Methodology for Inductor-Integrated Litz-Wired High-Power Medium-Frequency Transformer With the

Nanocrystalline Core Material for Isolated DC-Link Stage of Solid-State Transformer. *IEEE Transactions on Power Electronics*, 35(11):11557–11573, November 2020.

[11] J. Reinert, A. Brockmeyer, and R.W.A.A. De Doncker. Calculation of losses in ferro- and ferrimagnetic materials based on the modified Steinmetz equation. *IEEE Transactions on Industry Applications*, 37(4):1055–1061, July 2001.

[12] J. Muhlethaler, J. Biela, J. W. Kolar, and A. Ecklebe. Core Losses Under the DC Bias Condition Based on Steinmetz Parameters. *IEEE Transactions on Power Electronics*, 27(2):953–963, February 2012.

[13] Jieli Li, T. Abdallah, and C.R. Sullivan. Improved calculation of core loss with nonsinusoidal waveforms. In *Conference Record of the 2001 IEEE Industry Applications Conference. 36th IAS Annual Meeting (Cat. No.01CH37248)*, volume 4, pages 2203–2210 vol.4, September 2001. ISSN: 0197-2618.

[14] William G. Hurley, Maeve C. Duffy, Jesus Acero, Ziwei Ouyang, and Jun Zhang. 17 - Magnetic Circuit Design for Power Electronics. In Muhammad H. Rashid, editor, *Power Electronics Handbook (Fourth Edition)*, pages 571–589. Butterworth-Heinemann, January 2018.

[15] Fausto Fiorillo, Giorgio Bertotti, Carlo Appino, and Massimo Pasquale. Soft Magnetic Materials. In *Wiley Encyclopedia of Electrical and Electronics Engineering*, pages 1–42. John Wiley & Sons, Inc., Hoboken, NJ, USA, December 1999.

[16] British Standards Institution. *Ferrite cores. Guidelines on dimensions and the limits of surface irregularities. Part 8, Part 8,.* 2019. OCLC: 1197739030.

[17] Fabio Freschi and Maurizio Repetto. VIS: An artificial immune network for multi-objective optimization. *Engineering Optimization*, 38(8):975–996, December 2006.

[18] K. Deb, A. Pratap, S. Agarwal, and T. Meyarivan. A fast and elitist multiobjective genetic algorithm: NSGA-II. *IEEE Transactions on Evolutionary Computation*, 6(2):182–197, April 2002.

[19] James Cale, Scott D. Sudhoff, and Ricky R. Chan. Ferrimagnetic Inductor Design Using Population-Based Design Algorithms. *IEEE Transactions on Magnetics*, 45(2):726–734, February 2009.

[20] Grzegorz Dudek. An Artificial Immune System for Classification With Local Feature Selection. *IEEE Transactions on Evolutionary Computation*, 16(6):847–860, December 2012.

[21] S. Musumeci, L. Solimene, C. Ragusa, M. Palma, and O. de la Barriere. Saturable Inductor Modelling in GaN FETs Based Synchronous Buck Converter. In *2020 International Symposium on Power Electronics, Electrical Drives, Automation and Motion (SPEEDAM)*, pages 396–401, June 2020.

[22] M. Lodi, A. Oliveri, and M. Storace. A low-cost online estimator for switch-mode power supplies with saturating ferrite-core inductors. In *2019 26th IEEE International Conference on Electronics, Circuits and Systems (ICECS)*, pages 851–854, November 2019.

[23] L. Solimene, S. Musumeci, and C. Ragusa. Saturable Ferrite Inductor Parameters Obtained Through a Double Step Optimization. In *2020 55th International Universities Power Engineering Conference (UPEC)*, pages 1–6, September 2020.

[24] Giulia Di Capua and Nicola Femia. A Novel Method to Predict the Real Operation of Ferrite Inductors With Moderate Saturation in Switching Power Supply Applications. *IEEE Transactions on Power Electronics*, 31(3):2456–2464, March 2016.

[25] Kateryna Stoyka, Nicola Femia, and Giulia Di Capua. Power Inductors Behavioral Modeling Revisited. *IEEE Transactions on Circuits and Systems I: Regular Papers*, 67(12):5636–5649, December 2020.

[26] Hilmi Gurleyen, Erkan Mese, Ju Hyung Kim, and Bulent Sarlioglu. Nonlinear analytical model of an inductance considering saturation and temperature variation. In *2017 IEEE Energy Conversion Congress and Exposition (ECCE)*, pages 3150–3154, October 2017.

[27] D. Scirè, S. Rosato, G. Lullo, and G. Vitale. A Temperature Dependent Non-Linear Inductor Model for a DC/DC Boost Converter. In *2018 15th International Conference on Synthesis, Modeling, Analysis and Simulation Methods and Applications to Circuit Design (SMACD)*, pages 237–9, July 2018.

[28] A. Oliveri, G. Di Capua, K. Stoyka, M. Lodi, M. Storace, and N. Femia. A Power-Loss-Dependent Inductance Model for Ferrite-Core Power Inductors in Switch-Mode Power Supplies. *IEEE Transactions on Circuits and Systems I: Regular Papers*, 66(6):2394–2402, June 2019.

[29] Salvatore Musumeci, Luigi Solimene, and Carlo Stefano Ragusa. Identification of DC Thermal Steady-State Differential Inductance of Ferrite Power Inductors. *Energies*, 14(13):3854, January 2021.

[30] L. Solimene, C. Ragusa, S. Musumeci, O. de la Barrière, and F. Fiorillo. Modeling of Saturable Inductors for Application in DC-DC Converters. In *2019 26th IEEE International Conference on Electronics, Circuits and Systems (ICECS)*, pages 839–842, November 2019.

[31] Carlo Ragusa, Luigi Solimene, Salvatore Musumeci, Olivier de la Barriere, Fausto Fiorillo, Giulia Di Capua, and Nicola Femia. Computation of current waveform in ferrite power inductors for application in buck-type converters. *Journal of Magnetism and Magnetic Materials*, 502:166458, May 2020.

[32] Alaa Hilal, Marie Ange Raulet, and Christian Martin. Magnetic Components Dynamic Modeling With Thermal Coupling for Circuit Simulators. *IEEE Transactions on Magnetics*, 50(4):1–4, April 2014.

[33] P.R. Wilson, J.N. Ross, and A.D. Brown. Simulation of magnetic component models in electric circuits including dynamic thermal effects. *IEEE Transactions on Power Electronics*, 17(1):55–65, January 2002.

[34] Sadeq Ali Qasem Mohammed and Jin-Woo Jung. A Comprehensive State-of-the-Art Review of Wired/Wireless Charging Technologies for Battery Electric Vehicles: Classification/Common Topologies/Future Research Issues. *IEEE Access*, 9:19572–19585, 2021.

[35] Vincenzo Cirimele, Michela Diana, Fabio Freschi, and Massimo Mitolo. Inductive Power Transfer for Automotive Applications: State-of-the-Art and Future Trends. *IEEE Transactions on Industry Applications*, 54(5):4069–4079, September 2018.

[36] Wenzheng Xu, Weifa Liang, Jian Peng, Yiguang Liu, and Yan Wang. Maximizing Charging Satisfaction of Smartphone Users via Wireless Energy Transfer. *IEEE Transactions on Mobile Computing*, 16(4):990–1004, April 2017.

[37] Eun S. Lee, Byeong G. Choi, Myung Y. Kim, and Seung H. Han. Optimal Number of Turns Design of the IPT Coils for Laptop Wireless Charging. *IEEE Access*, 9:19548–19561, 2021.

[38] Junfeng Yang, Xiaodong Zhang, Kaijian Zhang, Xiaoyan Cui, Chaoqun Jiao, and Xu Yang. Design of LCC-S Compensation Topology and Optimization of Misalignment Tolerance for Inductive Power Transfer. *IEEE Access*, 8:191309–191318, 2020.

[39] Wenbo Wang, Junjun Deng, Deliang Chen, Zhenpo Wang, and Shuo Wang. A Novel Design Method of LCC-S Compensated Inductive Power Transfer System Combining Constant Current and Constant Voltage Mode via Frequency Switching. *IEEE Access*, 9:117244–117256, 2021.

[40] Yuqi Wei, Quanming Luo, and Alan Mantooth. Comprehensive analysis and design of LLC resonant converter with magnetic control. *CPSS Transactions on Power Electronics and Applications*, 4(4):265–275, December 2019.

[41] Yuqi Wei, Quanming Luo, Xiong Du, Necmi Altin, J. Marcos Alonso, and Homer Alan Mantooth. Analysis and Design of the LLC Resonant Converter With Variable Inductor Control Based on Time-Domain Analysis. *IEEE Transactions on Industrial Electronics*, 67(7):5432–5443, July 2020.

[42] W.H. Wolfle and W.G. Hurley. Quasi-active power factor correction with a variable inductive filter: theory, design and practice. *IEEE Transactions on Power Electronics*, 18(1):248–255, January 2003.

[43] J. Marcos Alonso, Marina Perdigão, Marco A. Dalla Costa, Shu Zhang, and Yijie Wang. Variable inductor modeling revisited: The analytical approach. In *2017 IEEE Energy Conversion Congress and Exposition (ECCE)*, pages 895–902, October 2017.

[44] British Standards Institution and British Standards Institution. *Glossary of electrotechnical, power, telecommunication, electronics, lighting and colour terms. Part 1. Group 07. Part 1. Group 07.* British Standards Institution, London, 1991. OCLC: 958836520.

[45] Luigi Solimene, Fabio Corti, Salvatore Musumeci, Carlo Stefano Ragusa, Alberto Reatti, and Ermanno Cardelli. Design and modelling of a controlled saturable inductor for an LCC-S compensated WPT system. *Journal of Magnetism and Magnetic Materials*, 564:170056, December 2022.

[46] Ned Mohan, Tore M. Undeland, and William P. Robbins. *Power electronics: converters, applications, and design*. John Wiley & Sons, Hoboken, NJ, 3rd ed edition, 2003.

[47] Korawich Niyomsatian, Johan J. C. Gyselinck, and Ruth V. Sabariego. Experimental Extraction of Winding Resistance in Litz-Wire Transformers—Influence of Winding Mutual Resistance. *IEEE Transactions on Power Electronics*, 34(7):6736–6746, July 2019.

[48] Nong Wang, Zhonghua Zhang, Bing Han, Zhengkun Li, and Yunfeng Lu. A 250 mA high-precision DC current source with improved stability for the Joule Balance at NIM. In *29th Conference on Precision Electromagnetic Measurements (CPEM 2014)*, pages 644–645, August 2014. ISSN: 2160-0171.

[49] Nong Wang, Yang Zhang, Zhengkun Li, and Zhonghua Zhang. A DCCT-based 100-A DC current source with high stability. In *2016 Conference on Precision Electromagnetic Measurements (CPEM 2016)*, pages 1–2, July 2016. ISSN: 2160-0171.

[50] E. Armando, F. Fusillo, S. Musumeci, and F. Scrimizzi. Low Voltage Trench-Gate MOSFETs for High Efficiency Auxiliary Power Supply Applications. In *2019 International Conference on Clean Electrical Power (ICCEP)*, pages 165–170, Otranto, Italy, July 2019. IEEE.

[51] Vincenzo Barba, Luigi Solimene, Marco Palma, Salvatore Musumeci, Carlo Stefano Ragusa, and Radu Bojoi. Modelling and Experimental Validation of GaN Based Power Converter for LED Driver. In *2022 IEEE International Conference on Environment and Electrical Engineering and 2022 IEEE Industrial and Commercial Power Systems Europe (EEEIC / I&CPS Europe)*, pages 1–6, Prague, Czech Republic, June 2022. IEEE.

[52] Cédric Lecluyse, Ben Minnaert, and Michael Kleemann. A Review of the Current State of Technology of Capacitive Wireless Power Transfer. *Energies*, 14(18):5862, January 2021. Number: 18 Publisher: Multidisciplinary Digital Publishing Institute.

[53] Jiejian Dai and Daniel C. Ludois. A Survey of Wireless Power Transfer and a Critical Comparison of Inductive and Capacitive Coupling for Small Gap Applications. *IEEE Transactions on Power Electronics*, 30(11):6017–6029, November 2015.

[54] Luigi Solimene, Fabio Corti, Salvatore Musumeci, Alberto Reatti, and Carlo Ragusa. Extended ZVS/ZCS operation of Class-E Inverter for Capacitive Wireless Power Transfer. In *2022 IEEE International Conference on Environment and Electrical Engineering and 2022 IEEE Industrial and Commercial Power Systems Europe (EEEIC / I&CPS Europe)*, pages 1–6, Prague, Czech Republic, June 2022. IEEE.

[55] Fabio Corti, Alberto Reatti, Ya-Hui Wu, Dariusz Czarkowski, and Salvatore Musumeci. Zero Voltage Switching Condition in Class-E Inverter for Capacitive Wireless Power Transfer Applications. *Energies*, 14(4):911, January 2021.